Multi-Resolution-Analysis Scheme for Uncertainty Quantification in Chemical Systems[☆]

O. P. Le Maître[a], H. N. Najm[b], P. P. Pébay[b], R. G. Ghanem[c], O. M. Knio[c]

[a] *Centre d'Etudes de Mécanique d'Île de France, Université d'Evry Val d'Essonne, 91020 Evry, France*
[b] *Combustion Research Facility, Sandia National Laboratories, Livermore, CA 94550, USA*
[c] *Aerospace and Mechanical Engineering Department, University of South Californie, Los Angeles, CA 90089, USA*
[d] *Department of Mechanical Engineering, The Johns Hopkins University, Baltimore, MD 21218, USA*

Abstract

This paper presents a multi-resolution approach for the propagation of parametric uncertainty in chemical systems. It is motivated by previous studies where Galerkin formulations of Wiener-Hermite expansions were found to fail in presence of steep dependences of the species concentrations with regard to the reaction rates. The multi-resolution scheme is based on representation of the uncertain concentration in terms of compact polynomial multi-wavelets, allowing for the control of the convergence in terms of polynomial order and resolution level. The resulting representation is shown to greatly improve the robustness of the Galerkin procedure in presence of steep dependences. However this improvement comes with a higher computational cost which drastically increases with the number of uncertain reaction rates. To overcome this drawback an adaptive strategy is proposed to control locally (in the parameter space) and in time the resolution level. The efficiency of the method is demonstrated for an uncertain chemical system having eight random parameters.

Key words: uncertainty quantification, chemical systems, polynomial chaos, multi-wavelets

1. Introduction

Quantification of uncertainty in the modeling of chemical systems is necessary for analysis, design and optimization purposes. It is also useful in the context of model validation with respect to experimental measurements that are generally imperfect and subject to systematic errors and noise. Numerical models aim to represent real physical processes, but are always approximations of the actual physics, involving both model and parametric uncertainties. Model uncertainty caused by modeling approximations will not be discussed here. Rather, we shall restrict ourselves to the uncertainty associated with the empirical physical parameters appearing in the simulation models (such as the reaction rate constants in chemical models). These physical parameters are usually extracted from (uncertain) experimental measurements, involving noise, by assuming an underlying chemical kinetic model. As a consequence, truly precise values are rarely available, and measured parameter values can strongly depend on the experimental conditions and apparatus used for their estimations. Thus, a probabilistic characterization (uncertainty bars, likelihood, ...) of these parameters is more appropriate, and numerical techniques are called for to quantify the resulting uncertainties in the simulation output.

[☆] This work was supported by the Laboratory Directed Research and Development Program at Sandia National Laboratories, funded by the US Department of Energy. Support was also provided by the Defense Advanced Research Projects Agency (DARPA) and Air Force Research Laboratory, Air Force Materiel Command, USAF, under agreement number F30602-00-2-0612. The U.S. government is authorized to reproduce and distribute reprints for Governmental purposes notwithstanding any copyright annotation thereon.

Email addresses: olm@limsi.fr (O. P. Le Maître), hnnajm@sandia.gov (H. N. Najm), pppebay@ca.sandia.gov (P. P. Pébay), ghanem@usc.edu (R. G. Ghanem), knio@jhu.edu (O. M. Knio)

A shorter version of this paper was published in J. Sci Comp., **29***:2, pp.864-889, (2007)*

Often, Monte Carlo (MC) techniques are used for analysis of parametric uncertainties. This approach involves performing a (pseudo) random sampling of the parameter distributions, followed by a statistical treatment of the corresponding set of simulations, yielding estimates of the expectation, moments and any desired statistics of the model output (see for instance [11, 14]. However, MC techniques are limited to simple models and/or rough estimates, due to the computational overhead required to solve the deterministic model multiple times. In fact, the large number of model realizations needed comes from the low convergence rate of the statistical estimates with regard to the size of the sample set. This fact strongly supports the use of deterministic techniques, as an alternative to MC sampling strategies. Among deterministic approaches, Polynomial Chaos (PC) expansions of the solution are attractive candidates, as they allow for a compact and convenient way of representing the functional dependences of the solution on the input random parameters.

PC methods have been the focus of many efforts within different fields of application (solid mechanics, thermal sciences, fluid flow,...) over the past decade, starting from the early work of Ghanem and Spanos[10]. The essence of these methods is the projection of the model output onto a subspace spanned by a basis of polynomial functions having for argument a denumerable set of independent random variables parameterizing the uncertain input data. For normalized Gaussian random variables one obtains the "classical" Wiener-Hermite expansion which has been generalized recently to other types of distributions by Karniadakis and co-workers [20]. First attempts to apply these techniques to the propagation of uncertainty in chemical and reacting flow models has been proposed in [18, 17, 7].

There are essentially two types of approaches for the determination of the spectral (projection) coefficients involved in the series expansion of the model output. In the first approach, orthogonality of the PC basis is exploited to perform a non-intrusive projection of the uncertain model solution: a sampling, either stochastic or deterministic, of the uncertainty range provides a set of model output values to be projected, *i.e.*, to compute the correlation between model output and basis polynomials. The second approach makes use of the mathematical model to derive a new set of equations -the spectral problem- through a Galerkin procedure, to be solved for the projection coefficients. The first approach is termed non-intrusive as it requires solving the deterministic model only, but for different values of the uncertain parameters. The second approach, termed intrusive, requires a reformulation of the deterministic model solution algorithm to handle the spectral problem. While more complex than the non-intrusive approach, the intrusive construction is potentially more efficient. However, the intrusive approach does yield a larger (compared to the original one) system of equations, and is particularly challenged by the non-linearities involved in chemical models [17, 8]. In fact, as shown in [17], even for simple reaction mechanisms, the intrusive spectral approach may fail to yield the correct solution because of truncation errors and lack of robustness. These issues are the central focus of the current paper.

The lack of robustness in intrusive spectral simulations is essentially due to (1) the loss of the "double infinity" limit of the polynomial chaos expansions because a single stochastic dimension is associated with each uncertain parameter, and (2) the decomposition of the solution using a basis of **global** polynomials, which appears to be inadequate when dealing with uncertain chemical systems: for sufficiently large uncertainty levels, the solution may exhibit strong dependence on the uncertain parameters (*e.g.* the reaction rates) leading to multi-modal probability density functions (PDFs). The requisite PC order necessary for representation of such solutions can be very high, so that truncated spectral computations break down due to numerical instabilities and aliasing errors. For example, the oscillatory nature of the polynomials can result in PC expansions for concentrations that contain negative valued realizations with non vanishing probability when truncated to finite order. Moreover, the use of high order expansions in spectral computations is not feasible in practice, due, first, to the emergence of numerical instability and, second, to the stiffness of the resulting system of equations whose time integration would require prohibitively small time-steps [17]. To address these limitations, we propose here to substitute the PC representation of chemical kinetic models with a multi-resolution scheme based on the multi-wavelet (MW) construction of Alpert [3], following the methodology introduced in [12] for 0-order or Wiener-Haar expansions, and later extended to arbitrary polynomial order in [13]. These new representations have been designed to deal with steepness and bifurcations triggered by uncertainty; by allowing for discontinuous dependences and introducing the notion of localized decomposition and resolution level (scales), the MW are expected to be better suited for complex chemical reactions than the usual PC expansion.

The paper is organized as follows. Section 2 presents the Multi-Resolution Analysis (MRA) scheme and MW expansion. It starts with a short summary of the spectral stochastic formulation for uncertainty quantification in Sections 2.1-2.2. Details on the MRA scheme and the construction method for the MW basis are then provided in Sections 2.3–2.5. Section 2.6 offers a short discussion on the Galerkin derivation of the spectral problem and implementation details needed for the examples treated in the remaining sections. In Section 3, we focus on the simple test-problem proposed in [17] for which the Wiener-Hermite (WHe) expansion was found ineffective. The causes for the WHe expansion failure are first analyzed in Section 3.1. The results obtained using the MW expansion, for the same problem, are then presented in Section 3.2 and a numerical inspection of the convergence of the MW representation is given. In the remaining sections the MRA scheme is applied to a more complex chemical model. This model corresponds to the uncertain hydrogen oxidation mechanism described in [16] and briefly summarized in Section 4. In Section 5, the situation where only one of the reaction rate constants is uncertain is first considered. This reaction rate constant is selected as the one having the largest impact on the concentrations. Our objective here is to demonstrate the flexibility and robustness provided by the MW representation in adapting the polynomial order and resolution level to the actual solution of the problem. The results shown in Section 5 are achieved at the cost of a significant enrichment of the expansion basis, which in turn directly translates into significant computational overhead. As a consequence, an adaptive strategy where a controlled local level of resolution applies is called for. Such a strategy is developed in Section 6, based on an extension of the technique proposed in [13] for unsteady solutions. The effectiveness of the overall method (MRA plus adaptive scheme) is demonstrated for up to 8 uncertain reaction rate constants. Finally, major conclusions and proposed future developments and improvements are given in Section 7.

2. Multi-Resolution Analysis and Multi-Wavelet Basis

2.1. Spectral Stochastic Representations

Consider a generic equation governing a function $\mathcal{P}$ that depends on space ($\mathbf{x}$), time (t) and an initial random event (θ):

$$\mathcal{O}(\mathcal{P}(\mathbf{x},t,\theta),\mathbf{x},t,\kappa(\theta))=0, \tag{1}$$

where $\mathcal{O}$ is a non-linear operator with random parameters $\kappa(\theta)$. The spectral stochastic representations considered in this paper rely on an orthogonal Fourier-like decomposition of the solution process according to:

$$\mathcal{P}(\mathbf{x},t,\theta)=\sum_i \mathcal{P}_i(\mathbf{x},t)\Psi_i(\boldsymbol{\xi}(\theta)), \tag{2}$$

where the $\mathcal{P}_i(\mathbf{x},t)$'s are the (yet-to-be-determined) spectral coefficients, $\{\Psi_i\}_{i\in\mathbb{N}}$ is the spectral basis and $\boldsymbol{\xi}$ is a random vector having independent components. The orthogonality of the basis functions, as well as the equality in Eq. (2), holds in the mean square sense (for the sake of brevity, the dependency on θ is no longer made explicit):

$$(\forall (i,j)\in\mathbb{N}^2)\quad \langle\Psi_i(\boldsymbol{\xi})\Psi_j(\boldsymbol{\xi})\rangle=\delta_{ij}\left\langle\Psi_i^2(\boldsymbol{\xi})\right\rangle, \tag{3}$$

where the brackets denote the mathematical expectation. The expansion (2) is an orthogonal basis function representation of $\mathcal{P}$. This approach has lead to the concepts of Homogeneous Chaos and Polynomial Chaos (PC) expansions [19, 6, 10] when $\boldsymbol{\xi}$ is a Gaussian vector with independent components. It can also be extended to non-Gaussian measures [9, 20]. Due to the orthogonality of the basis functions, the spectral coefficients satisfy:

$$(\forall i\in\mathbb{N})\quad \mathcal{P}_i=\frac{\langle\mathcal{P}\Psi_i(\boldsymbol{\xi})\rangle}{\langle\Psi_i(\boldsymbol{\xi})\Psi_i(\boldsymbol{\xi})\rangle}. \tag{4}$$

In order to determine the solution $\mathcal{P}$ it is sufficient to determine the spectral coefficients, $\mathcal{P}_i$. Several approaches can be used to determine the $\mathcal{P}_i$'s. A simple approach is to use Monte Carlo sampling (e.g. [18]) or, alternatively, deterministic quadrature formulas (e.g. [15]). In both cases, the problem is reduced to repeated solutions of a deterministic problem corresponding to different realizations of $\boldsymbol{\xi}$. The ensemble of

realizations is then used to reconstruct the spectral coefficients. We refer to this approach as a non-intrusive spectral projection (NISP) because it enables immediate application of a deterministic solution scheme.

An alternative to MC and quadrature schemes is the Galerkin approach, where the expansion (2) is substituted into the governing equation (1) and orthogonal projections onto the basis functions are performed, resulting in the following system for the spectral coefficients:

$$(\forall j \in \mathbb{N}) \quad \left\langle \mathcal{O}\left(\sum_i \mathcal{P}_i(\mathbf{x},t)\Psi_i(\boldsymbol{\xi}), \mathbf{x}, t, \sum_k \kappa_k \Psi_k(\xi)\right)\Psi_j(\boldsymbol{\xi})\right\rangle = 0, \tag{5}$$

where $\sum_k \kappa_k \Psi_k$ is the spectral expansion of the random parameters; this expansion is known provided that the statistic of κ is prescribed. In the following, we introduce a multi-wavelet (MW) basis function expansion which overcomes some of the limitations of representations based on bases of smooth global polynomials, which have been shown to be impractical for the modeling of uncertain chemical systems with large uncertainty level [17]. To simplify the presentation, we first focus on the case of a one-dimensional random vector ξ; generalization to the multi-dimensional case is then addressed in subsection 2.5.

2.2. Change of Variable

Let $\mathrm{p}(\eta)$ denote the Cumulative Density Function CDF, giving the probability that $\xi \leq \eta$. As in [12], we assume that $\mathrm{p}(\eta)$ is a continuous, strictly increasing function of η over the interval $[a, b]$, where $a < b$ are two real numbers, possibly infinite, and that $\mathrm{p}(a) = 0$ and $\mathrm{p}(b) = 1$. Based on these properties of $\mathrm{p}(\eta)$, it follows that for all $r \in [0, 1]$ there is a unique $\eta \in [a, b]$, such that $\mathrm{p}(\eta) = r$. In addition, if x is a uniformly distributed random variable on $[0, 1]$, then $p^{-1}(x)$ is a random variable with values in $[a, b]$ having the same distribution as ξ [11]. Consequently, using the mappings $x = \mathrm{p}(\xi)$ and $\xi = \mathrm{p}^{-1}(x)$, we develop a representation of $\mathcal{P}$ in terms of $x = \mathrm{p}(\xi)$. To shorten the notation we shall write $x(\xi)$ (resp. $\xi(x)$) for $x = \mathrm{p}(\xi)$ (resp. $\xi = \mathrm{p}^{-1}(x)$).

2.3. Multi-Resolution Analysis

In this section, we recall some properties of the multi-wavelet bases introduced by Alpert [3] (see also [2]). The application to the representation of ODEs with random initial conditions is considered in section 2.4.

2.3.1. Vector Spaces

For $\mathrm{N_o} = 0, 1, \ldots$ and $k = 0, 1, 2, \ldots$, we define the space $\mathbf{V}_k^{\mathrm{N_o}}$ of piecewise-continuous polynomials according to:

$$\mathbf{V}_k^{\mathrm{N_o}} = \left\{ f : \mathrm{Supp}(f) = [0,1], \forall l \in \{0, \ldots, 2^k - 1\}\, f_{|]2^{-k}l, 2^{-k}(l+1)[} \in \mathbb{R}_{\mathrm{N_o}}[X] \right\}, \tag{6}$$

where $\mathrm{Supp}(f)$ and $\mathbb{R}_{\mathrm{N_o}}[X]$ respectively denote the support of f and the ring of degree $\mathrm{N_o}$ polynomials with real coefficients. In other words, the restriction of f to any interval $]2^{-k}l, 2^{-k}(l+1)[$ is such a polynomial function, and f vanishes outside of $[0, 1]$. Thus, $\mathbf{V}_k^{\mathrm{N_o}}$ has dimension $2^k(\mathrm{N_o} + 1)$ and $\mathbf{V}_0^{\mathrm{N_o}} \subset \mathbf{V}_1^{\mathrm{N_o}} \subset \cdots \subset \mathbf{V}_k^{\mathrm{N_o}} \subset \ldots$. Denoting by $\mathbf{V}^{\mathrm{N_o}}$ the union of all of spaces $\mathbf{V}_k^{\mathrm{N_o}}$, $\mathbf{V}^{\mathrm{N_o}} = \overline{\bigcup_{k\geq 0} \mathbf{V}_k^{\mathrm{N_o}}}$, [3], we remark that $\mathbf{V}^{\mathrm{N_o}}$ is dense in $L^2([0, 1])$ with respect to the norm $\|f\| = \langle f, f\rangle^{1/2}$ where

$$\langle f, g\rangle = \int_0^1 f(x)g(x)\mathrm{d}x \tag{7}$$

is the standard inner product in $L^2([0, 1])$. In addition, for any integer k, the subspace $\mathbf{W}_k^{\mathrm{N_o}}$, which we employ below as the Multi-Wavelet (MW) subspace, is defined as the orthogonal complement of $\mathbf{V}_k^{\mathrm{N_o}}$ in $\mathbf{V}_{k+1}^{\mathrm{N_o}}$; we write:

$$(\forall k \in \mathbb{N}) \quad \mathbf{V}_k^{\mathrm{N_o}} \oplus \mathbf{W}_k^{\mathrm{N_o}} = \mathbf{V}_{k+1}^{\mathrm{N_o}}, \quad \mathbf{W}_k^{\mathrm{N_o}} \perp \mathbf{V}_k^{\mathrm{N_o}}, \tag{8}$$

where $\oplus$ denotes direct sum of vector spaces. From this construction we have:

$$\mathbf{V}_0^{\mathrm{N_o}} \bigoplus_{k\in\mathbb{N}} \mathbf{W}_k^{\mathrm{N_o}} = L^2([0, 1]). \tag{9}$$

2.3.2. Multi-Wavelet Basis

Let $\{\psi_0, \psi_1, \ldots, \psi_{\mathrm{N_o}}\}$ be an orthonormal basis of $\mathbf{W}_0^{\mathrm{N_o}}$, where the ψ_i's are piecewise polynomial functions of degree less than or equal to $\mathrm{N_o}$. From the orthonormality condition, we have:

$$(\forall (i,j) \in \mathbb{N}^2) \quad \langle \psi_i(x), \psi_j(x) \rangle = \delta_{ij}. \tag{10}$$

Since $\mathbf{W}_0^{\mathrm{N_o}} \perp \mathbf{V}_0^{\mathrm{N_o}}$, the first $\mathrm{N_o}+1$ moments of the ψ_i vanish, i.e.

$$(\forall (i,j) \in \mathbb{N}^2, i < j \leq \mathrm{N_o}) \quad \langle \psi_j, x^i \rangle = 0. \tag{11}$$

Equations (10) and (11) result in a system of polynomial equations which is solved, yielding the $(\mathrm{N_o}+1)$ ψ_i functions (see [3]). The space $\mathbf{W}_k^{\mathrm{N_o}}$, whose dimension is $2^k(\mathrm{N_o}+1)$, is spanned by the multi-wavelets, ψ_{jl}^k, which are images of the ψ_i's by translations and dilations. The ψ_{jl}^k are given by:

$$(\forall (j,k,l) \in \mathbb{N}^3, j \leq \mathrm{N_o}, l < 2^k) \quad \psi_{jl}^k(x) = 2^{k/2}\psi_j(2^k x - l). \tag{12}$$

and their support is $\mathrm{Supp}(\psi_{jl}^k) = [2^{-k}l, 2^{-k}(l+1)]$. Due to the orthonormality of the ψ's, we have:

$$\left\langle \psi_{im}^k, \psi_{jn}^l \right\rangle = \delta_{ij}\delta_{mn}\delta_{kl}. \tag{13}$$

A basis $\{\phi_0, \ldots, \phi_{k-1}\}$ for $\mathbf{V}_0^k$ is then constructed, using rescaled Legendre polynomials. Denoting L_i as the Legendre polynomial [1] of degree i, defined over $[-1,1]$, we set:

$$(\forall i \in \mathbb{N}, i \leq \mathrm{N_o}) \quad \phi_i(x) = \frac{L_i(2x-1)}{l_i}, \tag{14}$$

where l_i is a normalization factor selected such that

$$(\forall (i,j) \in \mathbb{N}^2, i \leq \mathrm{N_o}, j \leq \mathrm{N_o}) \quad \langle \phi_i(x), \phi_j(x) \rangle = \delta_{ij}. \tag{15}$$

The space $\mathbf{V}_k^{\mathrm{N_o}}$, whose dimension is $2^k(\mathrm{N_o}+1)$, is spanned by the polynomials $\phi_{il}^k(x) = 2^{k/2}\phi_i(2^k x - l)$, for $i = 0, \ldots, \mathrm{N_o}$ and $l = 0, \ldots, 2^k - 1$, that are images of the ϕ_i's by translations and dilations.

2.3.3. MW Expansion

A function $f \in L^2([0,1])$ can be arbitrarily well approximated using the MRA scheme constructed above. We denote by $f^{\mathrm{N_o},\mathrm{N_r}}$ the projection of f on $\mathbf{V}_{\mathrm{N_r}}^{\mathrm{N_o}}$; we have:

$$f^{\mathrm{N_o},\mathrm{N_r}}(x) = \sum_{l=0}^{2^{\mathrm{N_r}}-1} \sum_{i=0}^{\mathrm{N_o}} \left\langle \phi_{il}^{\mathrm{N_r}}(x), f(x) \right\rangle \phi_{il}^{\mathrm{N_r}}(x) = \sum_{l=0}^{2^{\mathrm{N_r}}-1} \sum_{i=0}^{\mathrm{N_o}} \overline{f}_{il}^{\mathrm{N_r}} \phi_{il}^{\mathrm{N_r}}(x). \tag{16}$$

An alternative expression for $f^{\mathrm{N_o},\mathrm{N_r}}$, valid for all $\mathrm{N_r} \geq 1$, in terms of multi-wavelets is:

$$f^{\mathrm{N_o},\mathrm{N_r}}(x) = f^{\mathrm{N_o},0} + \sum_{k=0}^{\mathrm{N_r}-1} \sum_{l=0}^{2^k-1} \left(\sum_{i=0}^{\mathrm{N_o}} \mathrm{d}f_{il}^k \psi_{il}^k(x) \right). \tag{17}$$

This expression, with $f^{\mathrm{N_o},0}(x)$ evaluated from Eq. (16), provides the sought-after expansion of $f^{\mathrm{N_o},\mathrm{N_r}}(x)$ in terms of Legendre polynomials overlaid with a specified number of MW details. The MW coefficients $\mathrm{d}f_{il}^k$ appearing in Eq. (17) are given by:

$$\mathrm{d}f_{il}^k = \left\langle \left\{ f^{\mathrm{N_o},k+1} - f^{\mathrm{N_o},k} \right\}, \psi_{il}^k \right\rangle \tag{18}$$

Denoting by $\delta_{\mathrm{N_o},\mathrm{N_r}}$ the L^2-norm of the approximation error of f on $\mathbf{V}_{\mathrm{N_r}}^{\mathrm{N_o}}$:

$$\delta_{\mathrm{N_o},\mathrm{N_r}} = \left\langle f - f^{\mathrm{N_o},\mathrm{N_r}}, f - f^{\mathrm{N_o},\mathrm{N_r}} \right\rangle, \tag{19}$$

convergence is characterized by $\delta_{\mathrm{N_o},\mathrm{N_r}} \to 0$ when the polynomial order $\mathrm{N_o}$ (p convergence) and the number of resolution levels $\mathrm{N_r}$ (h convergence) tend to ∞.

2.4. Expansion of a process

Consider an ODE governing $\mathcal{P}$, that depends on a random variable ξ satisfying the assumptions of section 2.2. Further, we assume that $\mathcal{P}(\xi)$ has a second order moment. Using the change of variables introduced in section 2.2, we express $\mathcal{P}(\xi)$ in terms of $x = \mathrm{p}(\xi)$ as:

$$\mathcal{P}(\xi) = \mathcal{P}(\mathrm{p}^{-1}(x)) = \tilde{\mathcal{P}}(x(\xi)). \tag{20}$$

Introducing this change of variable, and taking into account that x is uniformly distributed on $[0,1]$, it is easy to show that $\tilde{\mathcal{P}}(x) \in L^2([0,1])$. Thus, $\tilde{\mathcal{P}}(x)$ can be expanded according to Eq. (17). This expansion can be recasted through convenient indexation as (see [12]) :

$$\mathcal{P}(\xi) = \tilde{\mathcal{P}}(x(\xi)) = \sum_{\lambda \in \diamondsuit} \tilde{\mathcal{P}}_\lambda W_\lambda(x(\xi)), \quad \diamondsuit \equiv \triangle \cup \triangle_0 \tag{21}$$

where

$$\begin{cases} W_\lambda(x) = \psi_\lambda(x) & \text{for } \lambda \in \triangle \equiv \big\{\lambda : \lambda = (\mathrm{N_o}+1)(2^k + l - 1) + i, \\ & \qquad (i,j,k) \in \mathbb{N}^3, i \le \mathrm{N_o}, j < 2^k\big\}, \\ W_\lambda(x) = \phi_{-1-\lambda}(x) & \text{for } \lambda \in \triangle_0 \equiv \{-\mathrm{N_o}-1, -\mathrm{N_o}, \ldots, -1\}. \end{cases} \tag{22}$$

The resolution level k for any $\lambda \in \triangle$ will be denoted by $|\lambda|$.

2.5. The Multi-Dimensional Basis

Extension of the 1D MW expansion to the $\mathrm{N_d}$-dimensional case is now considered. For simplicity, we focus on a vector $\boldsymbol{\xi}$ with random uncorrelated and independent components $\{\xi_1, \ldots, \xi_{\mathrm{N_d}}\}$:

$$\mathrm{pdf}(\boldsymbol{\xi}) = \prod_{d=0}^{\mathrm{N_d}} \mathrm{pdf}_d(\xi_d).$$

where pdf_d denotes the probability density function of ξ_d. For each component ξ_d the real numbers $a_d < b_d$ and assume that pdf_d satisfies the assumptions of 2.2. Then $\forall x_d \in [0,1]$ there is a unique $\xi_d \in [a_d, b_d]$, denoted for short $\xi_d(x_d)$, such that $\mathrm{p}_d(\xi_d) = x_d$. Consistent with the one-dimensional case, we write for short $\boldsymbol{\xi}(\boldsymbol{x}) = (\xi_1(x_1), \ldots, \xi_{\mathrm{N_d}}(x_{\mathrm{N_d}}))$ and $\boldsymbol{x}(\boldsymbol{\xi}) = (x_1(\xi_1), \ldots, x_{\mathrm{N_d}}(\xi_{\mathrm{N_d}}))$. We now consider the multi-index $\boldsymbol{\lambda} = (\lambda_1, \ldots, \lambda_{\mathrm{N_d}})$, and define the sets

$$\Lambda_k = \left\{ \boldsymbol{\lambda} : \sum_{d=1}^{\mathrm{N_d}} |\lambda_d| = k \right\}, \mathcal{W}_k = \left\{ \prod_{d=1}^{\mathrm{N_d}} W_{\lambda_d}(x_d) : \boldsymbol{\lambda} = (\lambda_1, \ldots, \lambda_{\mathrm{N_d}}) \in \Lambda_k \right\}. \tag{23}$$

$\mathcal{W}_k$ is the set of multidimensional multi-wavelets having resolution level k. Let $M_k = \mathrm{Card}(\Lambda_k)$, such that the MW expansion of $\tilde{\mathcal{P}}(\boldsymbol{x})$ can now be formally written as:

$$\tilde{\mathcal{P}}(\boldsymbol{x}) = \sum_{i=1}^{M_0} c_i^0 \Gamma_i^0(\boldsymbol{x}) + \sum_{i=1}^{M_1} c_i^1 \Gamma_i^1(\boldsymbol{x}) + \sum_{i=1}^{M_2} c_i^2 \Gamma_i^2(\boldsymbol{x}) + \ldots \tag{24}$$

where $\Gamma^k(\boldsymbol{x}) \in \mathcal{W}_k$ denotes a multidimensional multi-wavelet of resolution k. In practice, the MW expansion has to be truncated. For instance, we can choose to retain all multi-indices $\boldsymbol{\lambda}$ such that $|\boldsymbol{\lambda}| = \sum_{d=1}^{\mathrm{N_d}} |\lambda_d| \le \mathrm{N_r}$, where $\mathrm{N_r}$ is a prescribed resolution level. After truncation, the finite expansion may be rewritten in a single index form as:

$$\mathcal{P}(\boldsymbol{\xi}) = \tilde{\mathcal{P}}(\boldsymbol{x}(\boldsymbol{\xi})) \approx \sum_{i=0}^{\mathrm{Nw}} \tilde{\mathcal{P}}_i \mathcal{M}_i(\boldsymbol{x}(\boldsymbol{\xi})), \tag{25}$$

where $\mathrm{Nw} + 1 = \sum_{i=0}^{\mathrm{N_r}} M_i$ is the dimension of the truncated basis $\{\mathcal{M}_i, i = 0, \ldots, \mathrm{Nw}\}$. Further, we use the convention that the indexing is performed in such a way that the first element of the basis is $\mathcal{M}_0 = 1$. With this convention, the mean and variance of $\mathcal{P}(\boldsymbol{\xi})$ are respectively given by:

$$\langle \mathcal{P} \rangle = \tilde{\mathcal{P}}_0, \quad \sigma^2(\mathcal{P}) = \sum_{i=1}^{\mathrm{Nw}} \tilde{\mathcal{P}}_i^2.$$

2.6. Galerkin Projection Schemes

When an intrusive approach is used, the spectral coefficients appearing in the MW expansion of the process $\tilde{\mathcal{P}}(\boldsymbol{x})$ are determined using the Galerkin projection technique outlined in section 2.1. However, the projection of the governing equations on the spectral basis, as given by Eq. (5), may raise several difficulties depending on the nature of the non-linear operator $\mathcal{O}$. For instance, in chemical systems, one has to deal with both polynomial and non-algebraic functionals in the determination of the chemical source terms. The general spectral treatment of uncertain chemical source terms was extensively discussed in [17], and we only detail here the non-linearities appearing in the computational examples presented in the following, namely binary and ternary products of uncertain quantities. For other types of non-linearities (*e.g.* non-algebraic terms such as exp, log, square root, ...), the reader should consult [17, 7, 8] since the methodologies readily extend to the MW expansions.

In this work, we have to evaluate the spectral coefficients $(ab)_i$ and $(abc)_i$ of binary and ternary products respectively of uncertain quantities a, b and c (for instance a is a reaction rate and b and c two species concentrations), knowing their MW expansions:

$$a = \sum_{i=0}^{\mathrm{Nw}} a_i \mathcal{M}_i, \quad b = \sum_{i=0}^{\mathrm{Nw}} b_i \mathcal{M}_i, \quad \text{and } c = \sum_{i=0}^{\mathrm{Nw}} c_i \mathcal{M}_i.$$

Clearly, $(ab)_i$ is given by:

$$(ab)_i = \langle ab, \mathcal{M}_i \rangle = \sum_{j=0}^{\mathrm{Nw}} \sum_{k=0}^{\mathrm{Nw}} a_j b_k \langle \mathcal{M}_j \mathcal{M}_k, \mathcal{M}_i \rangle = \sum_{j=0}^{\mathrm{Nw}} \sum_{k=0}^{\mathrm{Nw}} D_{ijk} a_j b_k,$$

where we have denoted by $D_{ijk} = \langle \mathcal{M}_j \mathcal{M}_k, \mathcal{M}_i \rangle$ the components of the binary product tensor D. The components of D are independent of a and b, and are only functions of the basis. Thus, D is computed once and stored for subsequent use. It has to be mentioned that D is sparse, thanks to the orthogonality of the MW basis functions. A similar Galerkin projection can be used to compute the spectral coefficients of ternary products (abc). It yields the ternary product tensor $T_{ijkl} = \langle \mathcal{M}_j \mathcal{M}_k \mathcal{M}_l, \mathcal{M}_i \rangle$:

$$(abc)_i = \sum_{j=0}^{\mathrm{Nw}} \sum_{k=0}^{\mathrm{Nw}} \sum_{l=0}^{\mathrm{Nw}} T_{ijkl} a_j b_k c_l.$$

However, even if T_{ijkl} is again a sparse tensor, the number of arithmetic operations required by the application of the previous expression may be prohibitive for large $\mathrm{N_r}$ and/or $\mathrm{N_o}$. In that case, a pseudo-spectral approximation based on the application of two successive binary products is preferred:

$$(abc)_i = \sum_{j=0}^{\mathrm{Nw}} \sum_{k=0}^{\mathrm{Nw}} D_{ijk} (ab)_j c_k, \quad \text{where } (ab)_j = \sum_{l=0}^{\mathrm{Nw}} \sum_{m=0}^{\mathrm{Nw}} D_{jlm} a_l b_m.$$

The pseudo-spectral approximation of ternary products yields significant reduction of the computational load, but introduces aliasing errors caused by the truncation of (ab) at the intermediate step. In general, the impact of these aliasing errors has to be carefully analyzed and controlled.

3. Comparison of WHe and MW Expansions

The purpose of this section is to examine the efficiency and robustness of the MW representation, compared to a global WHe expansion [19, 6, 10]. To this end, a simple problem is used, namely that proposed in [17]. In section 3.1, we demonstrate the limitation of the WHe expansion for this simple problem. Next (section 3.2) MW expansions are considered and their efficiency is contrasted with that of

WHe expansions. The test-problem is now introduced. Consider an uncertain system described by a state variable $X \in \mathbb{R}$ obeying:

$$\begin{cases} \dfrac{\mathrm{d}X}{\mathrm{d}t} = -X(X-B)(X-C), \\ X = X_0 \quad \text{for } t = 0, \end{cases} \tag{26}$$

where $B < 0$ and $C > 0$ are two real constants, and the initial condition X_0 is uncertain. The system has three fixed-points, $X = 0$, B and C, the first one being unstable. In the following, we set $B = -6$ and $C = 1$. While very simple, this problem is challenging for PC expansions whenever the initial condition is such the set of possible realizations of X_0 overlaps the unstable point. In this case, the set of realizations splits into two parts, depending on the sign of X_0, leading to a discontinuous solution as time advances. This discontinuity in the solution is a source of breakdown of the spectral representation, when using a global smooth basis.

3.1. Wiener-Hermite expansion

To start with, we consider the case where $X_0 \sim \mathcal{N}(\mu_0, \sigma_0^2)$, *i.e.*, the distribution of X_0 is Gaussian with mean μ_0 and standard deviation σ_0, where $\mu_0 \geq 0$ and $\sigma_0 > 0$ are two arbitrary real constants. Hence, the parametric representation of X_0 in terms of a normalized Gaussian variable ξ is:

$$X_0(\xi) = \mu_0 + \sigma_0 \xi, \quad \xi \sim \mathcal{N}(0,1). \tag{27}$$

Also, the solution $X(t,\xi)$ has a WHe PC expansion up to the order $\mathrm{N_o}$ given by:

$$X(t,\xi) = \sum_{k=0}^{\mathrm{N_o}} X_k(t) \Psi_k^{(H)}(\xi),$$

where the basis functions $\Psi_k^{(H)}(\xi)$ are the Hermite polynomials with respective degrees k [1]. To solve this problem, the Galerkin method described in section 2.6 is employed with a fourth order Runge-Kutta scheme using a time step $\Delta t = 10^{-3}$.

For a fixed order $\mathrm{N_o} = 5$, the numerical experiments presented in Figure 1 show that if the probability of $X_0 < 0$ is significant (for instance for $\sigma_0 = 0.4$ and 0.1), then all the realizations identically (with unit probability) end on the negative stable fixed-point. In contrast, if the probability of $X_0 < 0$ is small enough (for example $\sigma_0 = 0.05$), one obtains $\lim_{t\to\infty} X(t) = C$. This result contradicts the exact expected behavior: $\lim_{t\to\infty} X(t) = B$ if $X_0(\theta) < 0$ and $\lim_{t\to\infty} X(t) = C$ if $X_0(\theta) > 0$. Further, fixing $\mu_0 = 0.2$ and $\sigma_0 = 0.1$, and increasing the expansion order from $\mathrm{N_o} = 1$ to 7, we observe that the positive stable fixed-point is selected for $\mathrm{N_o} \leq 2$, while the solution goes to the negative fixed-point for $3 \leq \mathrm{N_o} \leq 7$; worst, increasing further $\mathrm{N_o}$ leads to unstable computations.

This simple problem may be viewed as a "prototype" for chemical reaction models, with X being identified with the "concentration" of the species of interest and $-B$ and C the constant "concentrations" of two intermediate species. First, if X is really considered as a concentration, X_0 should be positive with probability 1, as well as $X(t)$, and it is fundamental that the numerical method preserves the positivity of the random concentration $X(t)$ even for large variance of the solution. Second, if we allow the "concentration" X to be negative, the model can be understood as a chemical system having two asymptotic steady states dependening of the composition of the initial mixture; many chemical systems present such behaviors, for instance in presence of ignition or extinction of the reaction depending on the mixture composition, and it is essential that the random model can capture such drastically different dynamics. To enforce a strictly positive initial condition, one often uses a log-normal rather than a Gaussian distribution; so let us select $X_0(\xi) = \exp(\beta(\xi))$, where $\beta(\xi) = \mu_\beta + \sigma_\beta \xi \sim \mathcal{N}(\mu_\beta, \sigma_\beta^2)$. As a result, the initial condition has the following 1D WHe expansion [9]:

$$X_0(\xi) = \exp\left(\mu_\beta + \frac{\sigma_\beta^2}{2}\right) = \sum_{k=0}^{\infty} \left\{ \frac{\sigma_\beta^k}{\left\langle {\Psi_k^{(H)}}^2 \right\rangle} \Psi_k^{(H)}(\xi) \right\} > 0 \quad \text{w.p.1.} \tag{28}$$

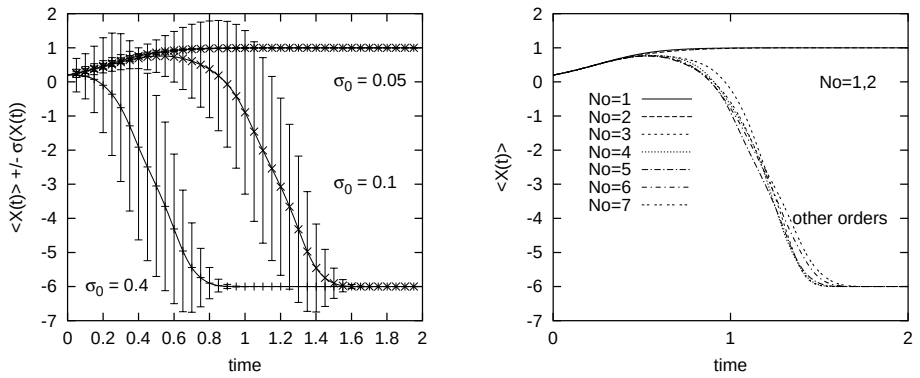

Figure 1: Time evolution of $X(t)$ for the test problem of section 3, using the WHe expansion and Gaussian initial condition: $X_0 \sim \mathcal{N}(\mu_0, \sigma_0^2)$. Left: results for $\mu_0 = 0.2$, 5th order expansion and $\sigma_0 = 0.4$, 0.1 and 0.05; plotted are the mean of $X(t)$ and error bar extending to $\pm\sigma(X(t))$. Right: mean of $X(t)$ for $\mu_0 = 0.2$, $\sigma_0 = 0.1$ and different expansion orders $\mathrm{N_o} = 1, \ldots, 7$. Computations for $\mathrm{N_o} > 7$ are unstable.

However, truncation of Eq. (28) to a finite order $\mathrm{N_o}$ may again introduce a non vanishing probability of having $X_0 < 0$. This issue was considered in [17], and we provide in Figure 2 the reconstruction of the parametric representation of X_0 in terms of ξ as given by Eq.(28), for different orders and $\mu_\beta = -2.5$, $\sigma_\beta = 1.1$. The plots show that while the 1D WHe expansion of $X_0(\xi)$ given by the truncated expansion (28) does converge to the exact mapping of the log-normal distribution for increasing $\mathrm{N_o}$, oscillations of the left tail around $X_0 = 0$ (see details on the right plot) lead to negative realizations for X_0. Moreover, these oscillations are damped with increasing frequency as $\mathrm{N_o}$ increases and occur for lower values of ξ, so they are more unlikely. However these oscillations around the unstable point have a dramatic impact on the model robustness: each point where the mapping crosses the axis $X_0 = 0$ induces a discontinuity in the solution $\lim_{t\to\infty} X(t)$, and so is a source for spectral breakdown. In other words, even though the probability of $X_0 < 0$ decreases for increasing $\mathrm{N_o}$, amplification of the higher order coefficients is expected because of the increasing number of zeros in the truncated mapping. This is evidenced in Figure 3, where the evolution of the mean and standard deviation of X with time are plotted, for different orders $\mathrm{N_o} = 1, \ldots, 7$. This time, only $\mathrm{N_o} = 2$ and 3 yield the correct long-time solution, while again computations with $\mathrm{N_o} \geq 8$ were found unstable. Also, the exact long-time solution of Eq.(26) is achieved for $\mathrm{N_o} = 2$ and 3; a prediction that is in fact inconsistent with the actual truncated initial condition used for the simulation, which should lead to a partition of the realization set between the two stable fixed-points.

3.2. Multi-Wavelet expansion

We repeat the experiments of the previous section using the MW expansion. The solution (and initial condition) are now expanded in terms of $x = \mathrm{p}(\xi)$, with $\xi \sim \mathcal{N}(0, 1)$:

$$X(t, \xi) = \tilde{X}(t, x = \mathrm{p}(\xi)) = \sum_{i=0}^{\mathrm{Nw}} \tilde{X}_i(t) \mathcal{M}_i(x). \tag{29}$$

For these tests, we select the Gaussian distribution of the initial condition $X_0 \sim \mathcal{N}(\mu_0, \sigma_0^2)$ and rely on Eq. (27) to determine the spectral coefficients of the initial condition:

$$(\tilde{X}_0)_i = \left\langle (\mu_0 + \sigma_0 \mathrm{p}^{-1}(x)), \mathcal{M}_i(x) \right\rangle = \mu_0 \delta_{i0} + \sigma_0 \int_0^1 \mathrm{p}^{-1}(x) \mathcal{M}_i(x) \mathrm{d}x. \tag{30}$$

To compute the integral appearing in the right-hand side of (30) high-order Gauss quadrature formulas [1] are used. However, since $\mathrm{p}^{-1}(x)$ is not a polynomial, $(\tilde{X}_0)_i$ can not be exactly computed from a Gauss

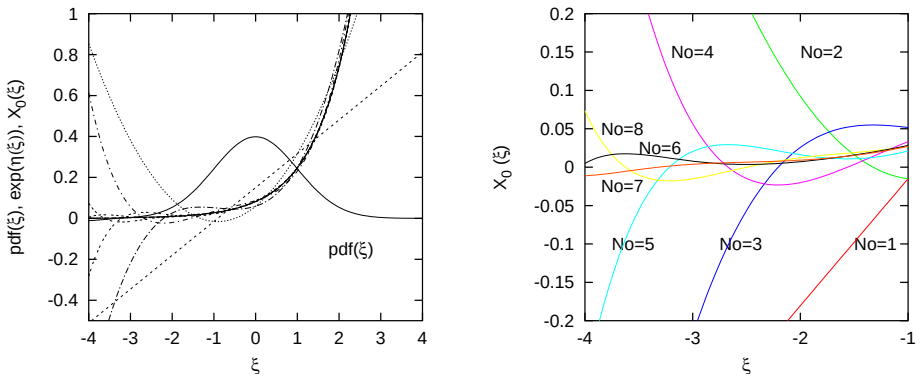

Figure 2: Left: WHe approximation of the parametric mapping of the log-normal distribution of $X_0(\xi)$ given by Eq. (28), for $\mu_\beta = -2.5$ and $\sigma_\beta = 1.1$, and with different orders of truncature. Also plotted are the pdf of ξ and the exact mapping ($N_o \to \infty$) in solid lines. Right: details of the mapping for $\xi \in [-4 : 1]$ showing the oscillations around $X_0 = 0$, for $N_o = 1, \ldots, 8$ as indicated.

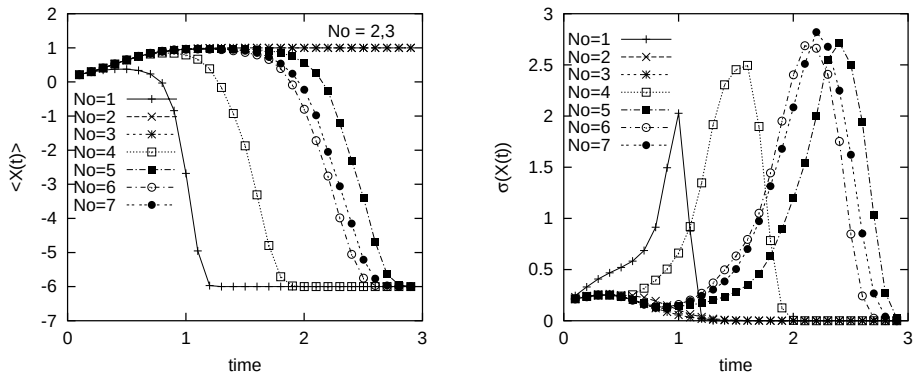

Figure 3: Time evolution of the computed mean (left) and standard deviation (right) of $X(t)$ for the test problem of section 3, using the WHe expansion with $N_o = 1, \ldots, 7$. log-normal initial condition with $\mu_\beta = -2.5$ and $\sigma_\beta = 1.1$.

quadrature. To minimize the quadrature error, 32 Gauss-points were used to estimate these integrals. We present in Figure 4 the resulting projection of $\tilde{X}(t = 0, x)$ using different resolution levels N_r and polynomial orders N_o, for $\mu_0 = 0.2$ and $\sigma_0 = 0.2$. The plots highlight the discontinuous character of the MW approximation, and its rate of convergence toward the exact mapping as both N_r and N_o increases. Further, it is shown that for fixed order N_o, the details at successive resolution levels are more and more focused on the tails of the distribution, *i.e.* at the MW supports for x in the neighborhood of 0 and 1. This behavior is expected because X, although integrable on $[0, 1]$, as shown in section 2.4, tends to $\pm\infty$ when x tends to 0 or 1.

Then, provided with the mapping of the initial condition, the governing equations for the MW coefficients are time integrated, still using the 4th order Runge-Kutta scheme with $\Delta t = 10^{-3}$, but employing the pseudo-spectral approximation of the ternary products (see section 2.6). The pseudo-spectral approximation was required here, because the size of the ternary product tensor would be too large for the largest values of N_o and N_r tested, even for sparse format storage. In Figures 5 and 6 we plot the time evolution of the computed mean and standard deviation of X for $N_o = 0, \ldots, 3$ and $N_r = 1, \ldots, 6$. The results illustrate that, for fixed N_o, both first and second order statistics converge for increasing N_r. In contrast with the WHe computations, the statistics converge to their "exact" values (available by sampling) and not to spurious ones. Specifically, all realizations point towards the negative or positive stable fixed-points depending on

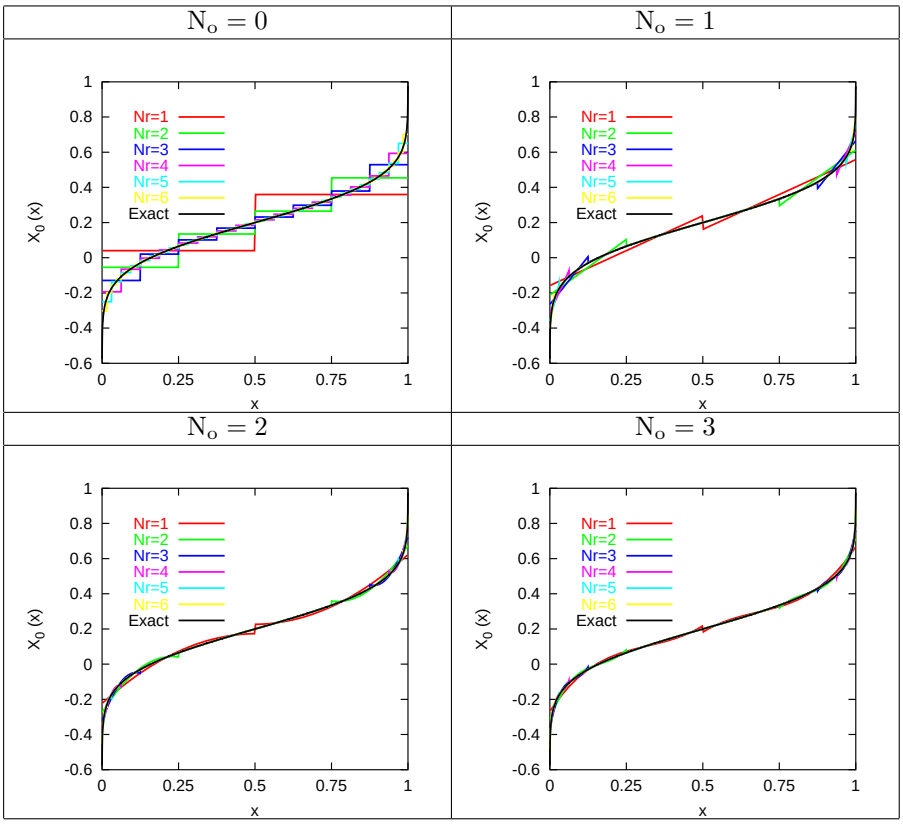

Figure 4: MW parametric mapping of $\tilde{X}_0(x)$ (Eq. (30)) for the Gaussian initial condition $X_0 \sim \mathcal{N}(0.2, 0.1^2)$; different orders N_o and resolution level N_r are presented as indicated.

their respective initial condition, and are not altogether trapped by one of the stable points. This behavior is clearly an improvement compared to the WHe case where computations, when stable, always predict vanishing standard deviation for long time. Moreover, it is found that the minimal resolution level to be used to satisfactorily capture the dynamics of X is roughly $N_r = 4$ for $N_o = 1, 3$ and $N_r = 5$ when using $N_o = 0, 2$.

To further understand the behavior of the MW expansion, we provide in Figure 7 reconstructions of the response-surfaces $\tilde{X}(t, x)$, for $N_o = 0$ and four values of N_r. It is shown that for $N_r = 1$, the model predicts that all realizations end on the positive stable point. This is consistent with the mapping of the actual initial condition of the simulation which for this low resolution level is positive $\forall x \in [0, 1]$ (see Fig. 4). For $N_r = 2$, Fig. 4 shows that the probability of realizations having negative initial condition will be overestimated: the computed mean of $X(t)$ presented in Fig. 5 reflects this fact, over-predicting the final negative mean, while the corresponding response-surface in Fig. 7 illustrates how the MW expansion can actually split the set of realizations consistently with the approximation of the initial condition. When N_r is increased further, the approximation of the initial mapping becomes better and better, the discontinuity point is found with greater and greater precision, and the transient dynamics of individual realizations improve (see Fig. 7).

Figure 8 depicts the response surfaces computed for $N_r = 4$ and $N_o = 0, \ldots, 3$. As explained above, this level of resolution provides quite an accurate estimate of the discontinuity location, but spurious oscillations in the solution are observed in the neighborhood of the discontinuity for $N_o > 0$, whose magnitudes increase with the polynomial order. These oscillations are in fact essentially due to Gibbs phenomena, characteristic of the representation of discontinuous solution using (even local) smooth polynomials. However, these oscillations are limited to the support overlapping the discontinuity, and do not contaminate the full uncertainty range. Hence, the contribution of the spurious oscillations to the statistics of the process decreases exponen-

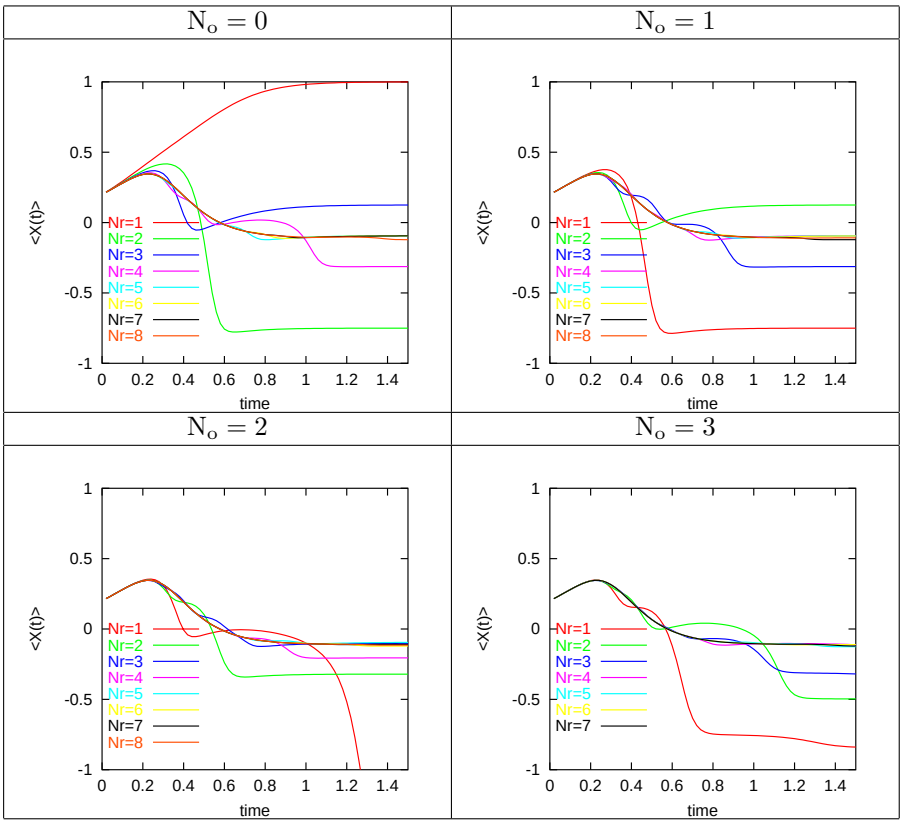

Figure 5: Time evolution of the computed mean of $X(t)$ for the MW expansions with N_o and N_r as indicated. The initial condition corresponds to the Gaussian distribution with $\mu_0 = 0.2$ and $\sigma_0 = 0.1$, whose corresponding MW approximations are plotted in Figure 4.

tially when the resolution level N_r increases, explaining the convergence, for $N_o > 0$, of the first and second order moments reported in Fig. 5 and 6. Clearly, these observations suggest that zero order polynomials should be used on supports overlapping discontinuities, and future work will focus on the adaptation of the local polynomial order with regard to the local behavior (smoothness) of the solution.

Repeating the experiment for the log-normal distribution of the previous subsection with the MW expansion (not shown) yields similar conclusions: correct long time solution for any resolution level and order, h and p convergence and more robustness compared to the WHe expansion. The results are not presented since in the following section we shall consider log-normal uncertainties in the context of (more complex) chemical system. To summarize the findings of the section, we stress that the MW expansion offers an attractive alternative to the WHe expansion in the context of chemical modeling, by providing more robustness and a better efficiency when dealing with steep or discontinuous processes. The MW expansion seems to be superior to WHe expansions when dealing with constrained problems, such as positivity of the solution, thanks to the local character of the representation. Moreover, by offering two ways of improving the predictions through increasing resolution level and polynomial order, the MW representation provides more flexibility than traditional global polynomial expansions with fixed dimension that can suffer from lack of robustness when increasing the representation order (recall, of course, that the general convergence of the PC representation is guaranteed only for increasing order *and* dimensionality). These claims are further investigated in the following sections.

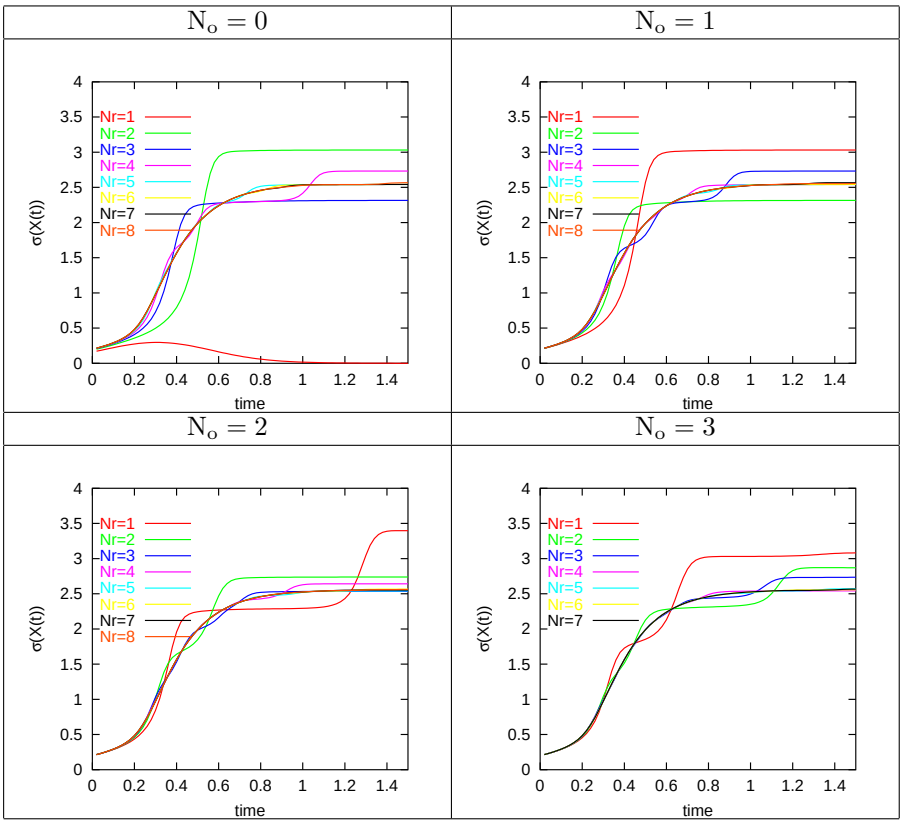

Figure 6: Time evolution of the computed standard deviation of $X(t)$ for the MW expansions with $\mathrm{N_o}$ and $\mathrm{N_r}$ as indicated. The initial condition corresponds to the Gaussian distribution with $\mu_0 = 0.2$ and $\sigma_0 = 0.1$, whose corresponding MW approximations are plotted in Figure 4.

4. Chemical Test Problem

4.1. Uncertainty Parameterization

In this section, we present a short description of the chemical model used in the remainder of this paper to test the efficiency of the proposed methods. This model is selected as it has been previously used as a test problem for uncertainty quantification in chemical system in [16, 18] and because spectral PC expansions are known to fail for this system. The model is a reduced hydrogen oxidation mechanism involving seven species (OH, H, H_2O, H_2, O_2, HO_2 and H_2O_2) and the eight reactions listed in Table 1 (see [16] for more details). The initial temperature and pressure are defined to be at supercritical conditions, and the overall oxidation process is assumed to be isothermal. For this chemical system, uncertainties in the forward reaction rates, $k_{f,j}$, are present: from experimental data, these uncertainties have been characterized in [16] by their median values $\hat{k}_{f,j}$ and respective uncertainty levels UF_j. It is assumed that the actual forward rates are contained, with 95% confidence level, within the lower and upper bounds $\hat{k}_{f,j}/UF_j$ and $\hat{k}_{f,j} \times UF_j$. Moreover, the forward reaction rates are modeled as independent random variables, and their probabilistic behaviors are modeled as log-normal distributions. It has to be noted that the assumption of independence is fairly strong but justified from the information theory point of view in the absence of any knowledge regarding the joint densities of the reaction rates : it yields the less informative probability law of the chemical model. From these assumptions, the eight forward rates can be parameterized using a set of eight independent normalized

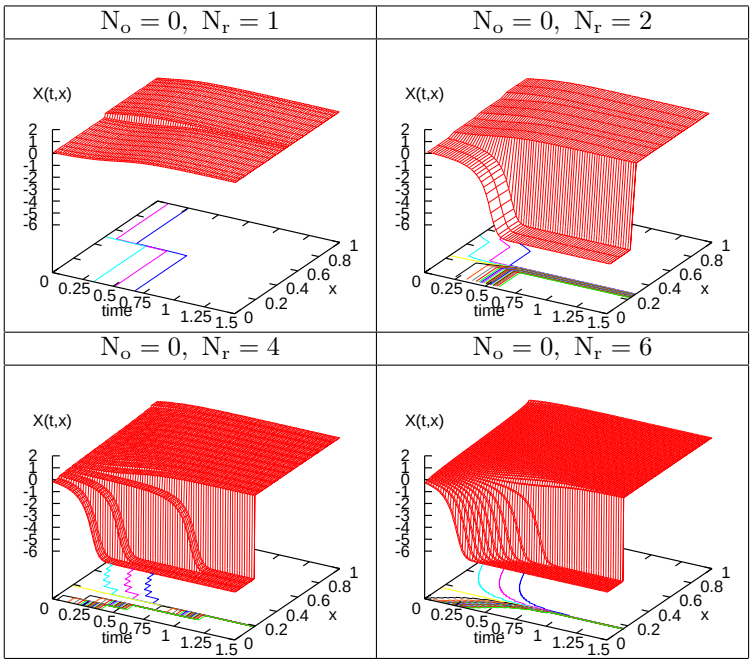

Figure 7: MW response-surfaces of $\tilde{X}(t,x)$ solution of the problem of section 3 and initial condition $X_0 \sim \mathcal{N}(0.2, 0.1^2)$. Plots were generated for $N_o = 0$ and $N_r = 1, 2, 4$ and 6 as indicated.

Gaussian variables $\boldsymbol{\xi} = (\xi_1, \ldots, \xi_8)$ according to:

$$(\forall (i,j) \in \{1,\ldots,8\}^2) \quad \left\{ \begin{array}{l} k_{f,j}(\xi_j) = \hat{k}_{f,j} \exp\left[\dfrac{\log(UF_j)}{1.96}\xi_j\right], \\ \xi_j \sim \mathcal{N}(0,1),\ \langle \xi_i \xi_j \rangle = \delta_{ij} \end{array} \right. \tag{31}$$

where [18, 17] the factor 1.96 ensures that the rate $k_{f,j}$ is in the range $[\hat{k}_{f,j}/UF_j, \hat{k}_{f,j} \times UF_j]$ with a probability equal to 0.95. The reverse rates are constructed from the equilibrium constants $K_{c,j}^{-1}$ of each of the eight reactions, which we presume to be known with unit probability. As a consequence, the reverse and forward rates are fully correlated and related by:

$$k_{r,j}(\xi_j) = k_{f,j}(\xi_j) \times K_{c,j}^{-1}, \tag{32}$$

The equilibrium constants are computed using the expected values of the heats of formation reported in Table 2 of [16] neglecting any uncertainty therein, and are listed in Table 1. From this parameterization of the reaction rates using the Gaussian vector $\boldsymbol{\xi}$, we deduce their MW expansions in terms of the random vector $\boldsymbol{x} = (x_1, \ldots, x_8)$ with independent components, all being uniformly distributed on $[0,1]$:

$$\tilde{k}_{f,j}(x_j) = k_{f,j}(\xi_j(x_j)) = \sum_{i=0}^{\mathrm{Nw}} \left(\tilde{k}_{f,j}\right)_i \mathcal{M}_i(\boldsymbol{x}), \quad \left(\tilde{k}_{f,j}\right)_i = \left\langle \tilde{k}_{f,j}, \mathcal{M}_i \right\rangle, \tag{33}$$

and similar expressions for the reverse rates.

4.2. Solution Method

The stochastic process to be modeled is then fully described by the time-evolution of the state vector containing the species concentrations:

$$\tilde{\mathcal{P}}(t,\boldsymbol{x}) = ([\mathrm{OH}](t,\boldsymbol{x}), [\mathrm{H}](t,\boldsymbol{x}), \ldots, [\mathrm{HO_2}](t,\boldsymbol{x}), [\mathrm{H_2O_2}](t,\boldsymbol{x}))^{\mathrm{T}}, \tag{34}$$

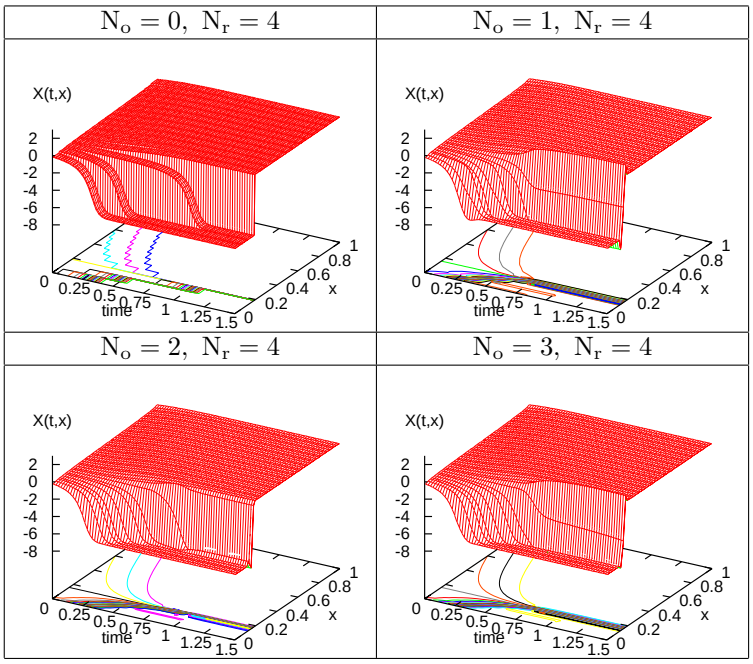

Figure 8: MW response-surfaces of $\tilde{X}(t,x)$ solution of the problem of section 3 and initial condition $X_0 \sim \mathcal{N}(0.2, 0.1^2)$. Plots were generated for $N_o = 0, \ldots, 3$ and $N_r = 4$ as indicated.

all having MW expansions of the form $\zeta(t,\boldsymbol{x}) = \sum_i \zeta_i(t)\mathcal{M}_i(\boldsymbol{x})$, where ζ is a "generic" component of $\tilde{\mathcal{P}}$. The chemical system is governed by the following system of coupled ODEs:

$$\frac{\mathrm{d}\tilde{\mathcal{P}}(t,\boldsymbol{x})}{\mathrm{d}t} = \mathcal{R}(\tilde{\mathcal{P}}(t,\boldsymbol{x}),\boldsymbol{x}), \tag{35}$$

where the right-hand side vector $\mathcal{R}$ is a non-linear functional of the uncertain species concentrations and reaction rates. For instance, the second component of $\tilde{\mathcal{P}}$ is governed by:

$$\begin{aligned}\frac{\mathrm{d}[\mathrm{H}](t,\boldsymbol{x})}{\mathrm{d}t} &= \Big\{\tilde{k}_{r,1}(\boldsymbol{x})[\mathrm{H_2O}](t,\boldsymbol{x}) + \tilde{k}_{f,2}(\boldsymbol{x})[\mathrm{H_2}](t,\boldsymbol{x})[\mathrm{OH}](t,\boldsymbol{x}) \\ &+ \tilde{k}_{r,3}(\boldsymbol{x})[\mathrm{HO_2}](t,\boldsymbol{x}) + \tilde{k}_{r,6}(\boldsymbol{x})[\mathrm{HO_2}](t,\boldsymbol{x})[\mathrm{H_2}](t,\boldsymbol{x})\Big\} \\ &- \Big\{\tilde{k}_{f,1}(\boldsymbol{x})[\mathrm{OH}](t,\boldsymbol{x})[\mathrm{H}](t,\boldsymbol{x}) + \tilde{k}_{r,2}(\boldsymbol{x})[\mathrm{H_2O}](t,\boldsymbol{x})[\mathrm{H}](t,\boldsymbol{x})\end{aligned}$$

j	Reaction			$\hat{k}_{f,j}$	$K_{c,j}$	UF_j
1	$OH + H$	$\longleftrightarrow$	H_2O	$1.479\ 10^{14}$	0	3.16
2	$H_2 + OH$	$\longleftrightarrow$	$H_2O + H$	$6.295\ 10^{11}$	$4.380\ 10^{-04}$	1.26
3	$H + O_2$	$\longleftrightarrow$	HO_2	$8.314\ 10^{13}$	$9.879\ 10^{-14}$	1.58
4	$HO_2 + HO_2$	$\longleftrightarrow$	$H_2O_2 + O_2$	$7.281\ 10^{11}$	$1.045\ 10^{-09}$	1.41
5	$H_2O_2 + OH$	$\longleftrightarrow$	$H_2O + HO_2$	$3.469\ 10^{12}$	$3.382\ 10^{-09}$	1.58
6	$H_2O_2 + H$	$\longleftrightarrow$	$HO_2 + H_2$	$1.696\ 10^{11}$	$7.723\ 10^{-06}$	2.00
7	H_2O_2	$\longleftrightarrow$	$OH + OH$	$3.993\ 10^{01}$	$1.589\ 10^{+11}$	3.16
8	$OH + H_2O$	$\longleftrightarrow$	$H_2O + O_2$	$3.917\ 10^{13}$	$3.534\ 10^{-18}$	3.16

Table 1: List of reactions and chemical data for the reduced hydrogen oxidation mechanism of [16]. $\hat{k}_{f,j}$ are the median forward rates, the $K_{c,j} = k_{f,j}/k_{r,j}$ are the (certain) equilibrium constants and the coefficients UF_j measure the uncertainty levels in each forward reaction rates as discussed in the text.

$$+ \quad \tilde{k}_{f,3}(\boldsymbol{x})[\mathrm{H}](t,\boldsymbol{x})[\mathrm{O_2}](t,\boldsymbol{x}) + \tilde{k}_{f,6}(\boldsymbol{x})[\mathrm{H_2O_2}](t,\boldsymbol{x})[\mathrm{H}](t,\boldsymbol{x})\Big\}. \tag{36}$$

Then, introduction of the MW expansions of the concentrations and reaction rates into the governing equations, followed by projection onto the spectral basis yields a system of $7(\mathrm{Nw}+1)$ ODEs for the MW coefficients, where we recall that $\mathrm{Nw}+1$ is the dimension of the MW basis. The equation for the i-th MW coefficient of [H] is, for instance :

$$\begin{aligned}\frac{\mathrm{d}[\mathrm{H}]_i}{\mathrm{d}t} = \quad &+ \quad (k_{r,1}[\mathrm{H_2O}] + k_{f,2}[\mathrm{H_2}][\mathrm{OH}] + k_{r,3}[\mathrm{HO_2}] + k_{r,6}[\mathrm{HO_2}][\mathrm{H_2}])_i \\ &- \quad (k_{f,1}[\mathrm{OH}][\mathrm{H}] + k_{r,2}[\mathrm{H_2O}][\mathrm{H}] + k_{f,3}[\mathrm{H}][\mathrm{O_2}] + k_{f,6}[\mathrm{H_2O_2}][\mathrm{H}])_i\,,\end{aligned} \tag{37}$$

which right-hand-side evaluation requires 2 binary and 6 ternary products. Due to the broad spectrum of time scales involved in this chemical system, the deterministic system of equations resulting from the Galerkin projection is stiff, as for the deterministic case. In the following, we shall make use of the software package DVODE of Brown, Hindmarsh and Byrne, designed for the integration of system of stiff ordinary differential equations [4, 5].

4.3. Initial conditions

To solve the chemical problem, initial conditions are needed. In this work, the initial concentrations are certain, and set to:

$$\begin{cases} [\mathrm{OH}] = [\mathrm{H}] = [\mathrm{HO_2}] = [\mathrm{H_2O_2}] = 0, \\ [\mathrm{H_2O}] = 4.281\ 10^{-3}, \quad [\mathrm{H_2}] = 2.06\ 10^{-6}, \quad [\mathrm{O_2}] = 1.04\ 10^{-6}. \end{cases}$$

Since these initial conditions are certain, their respective initial expansions are simply:

$$\begin{cases} [\mathrm{H_2O}](t=0,\boldsymbol{x}) = 4.281\ 10^{-3}\mathcal{M}_0, \\ [\mathrm{H_2}](t=0,\boldsymbol{x}) = 2.06\ 10^{-6}\mathcal{M}_0, \\ [\mathrm{O_2}](t=0,\boldsymbol{x}) = 1.04\ 10^{-6}\mathcal{M}_0. \end{cases}$$

The other species having all vanishing MW coefficients at $t=0$.

5. 1-D MW modeling of Supercritical Hydrogen Oxidation

Before considering the full set of stochastic dimensions, we restrict our attention to the case where only the seventh reaction rate constant is uncertain. Hence, the problem can be modeled with a single stochastic dimension, enabling intensive computations and analysis. Still, the uncertainty in $\tilde{k}_{f,7}$ and $\tilde{k}_{r,7}$ impacts the full set of species concentrations in a non-trivial way, as might be expected given the coupling of different species by the chemical source term, and as will be illustrated below. Before we start presenting these results, we recall that, for a given resolution level $\mathrm{N_r}$ and polynomial order $\mathrm{N_o}$, the dimension of the MW basis is $\mathrm{Nw}+1 = (\mathrm{N_o}+1)2^{\mathrm{N_r}}$.

5.1. Approximation of the reaction rates

As for the parameterization of the Gaussian distribution in the previous section, we provide in Figure 9 the MW approximations of the mapping for the log-normal distribution of the stochastic (uncertain) reaction rate $\tilde{k}_{f,7}$ (see Eq. (33)) obtained for different expansion orders and resolution levels. Since the mapping of the reaction rate in terms of the CDF $x(\xi)$ exhibits an infinite growth as $x \to 1$, it is seen that significant resolution is required to properly represent the distribution for the highest values of $\tilde{k}_{f,7}$. However, while the convergence of the mapping with increasing number of resolution levels is quite slow for the zero order expansion, very few levels are needed when using $\mathrm{N_o} = 2$ and 3. Also, it has to be noted that if the parameterization of the reaction rates is singular, yet integrable, it does not necessarily imply that such behavior is expected for the concentrations. Moreover, for unsufficient resolution level, discontinuities are expected to be present in the reaction rate mapping, due to the piecewise character of the expansion. These discontinuities in the reaction rate mapping are expected to affect in turn the continuity of concentration solution. These claims are verified in the following results.

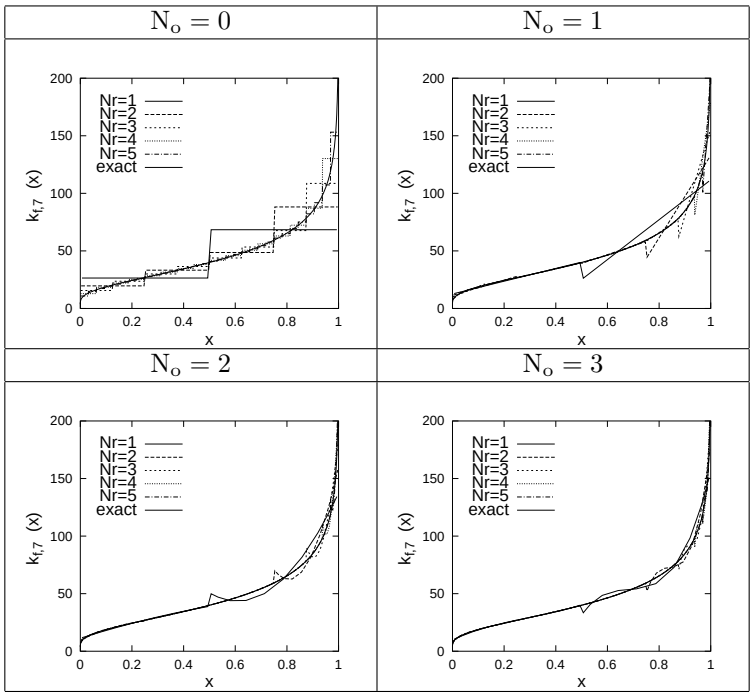

Figure 9: Parameterization of the log-normal forward rate $\tilde{k}_{f,7}$ as a function of $x = x(\xi)$, for $\mathrm{N_o} = 0, \ldots, 3$ and $\mathrm{N_r} = 1, \ldots, 5$ as indicated. Also plotted is the exact mapping.

5.2. First order moments

Figures 10 and 11 show the time evolution of the two first statistical moments of H concentration. Figure 10 displays the results obtained using straight-forward Monte-Carlo sampling (without NISP), with a 5000-point sample of $\tilde{k}_{f,7}$. On the other hand, Figure 11 shows the results obtained the intrusive MW approach, for $\mathrm{N_o} = 0, \ldots, 3$ and $\mathrm{N_r} = 1, \ldots, 5$. The former thus provides a baseline against which the latter can be compared.

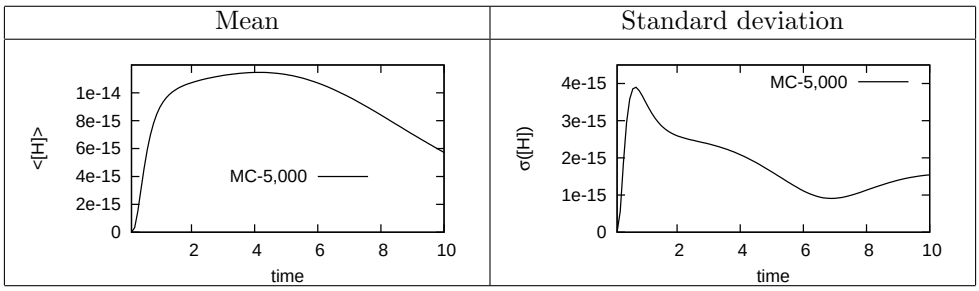

Figure 10: Mean (left) and standard deviation (right) of H concentration as a function of time. Computations with Monte-Carlo sampling using a 5000-point sample. Only the uncertainty in the 7-th reaction (see Table 1) is considered, all other forward rates being taken equal to their median values.

Focusing first on the zero-order case, *i.e.* Wiener-Haar expansion, depicted on the top row in the figure, the convergence of the solution when $\mathrm{N_r}$ increases is clearly visible. In fact, for the mean of $[\mathrm{H}](t)$, the solution obtained with $\mathrm{N_r} = 1$ is slightly over-estimated, but predictions for $\mathrm{N_r} \geq 2$ are hardly distinguishable in the plot, and in excellent agreement with the high order computations of the following rows. For the standard deviation, the convergence appears to be slower with $\mathrm{N_r}$, and the case with $\mathrm{N_r} = 1$ significantly underestimates the statistical dispersion of the concentration induced by the uncertainty. It even predicts the

absence of any uncertainty in the concentration for $t \approx 6.5$. This peculiar prediction will be explained later when analyzing the response-surfaces in Figure 14. Nonetheless, the convergence of the second order statistics, albeit slow, is still achieved for $N_o = 0$. Similar trends are reported when using $N_o = 1$, but with more accurate predictions for $N_r = 1$, and a faster convergence rate: for the mean H concentration the curves are nearly indistinguishable, and for the standard deviation, only the case for $N_r = 1$ has noticeable deviations from the predictions using higher resolution levels. For the last two orders tested ($N_o = 2, 3$, in the bottom lines of Fig. 11), even the predictions for $N_r = 1$ provide very accurate results, as far as these low order moments are concerned; a result that may be surprising considering the mapping of the corresponding reaction rates depicted in Figure 9. Increasing the level of resolution does not seem to bring additional significant information into the uncertain process, even if the quality of the mapping appears fairly poor for $N_r = 1$ and $N_o = 2$ and 3. In fact, a closer analysis (see below) of the supplementary details introduced when increasing the resolution level indicates that they do improve the representation, although their impact on the low-order statistics is negligible: a finer analysis of the predicted process distribution is necessary to assess the improvement resulting from increasing resolution. Last, but not least, we see a very good agreement between Monte-Carlo and MW results, agreement that improves as N_o increases.

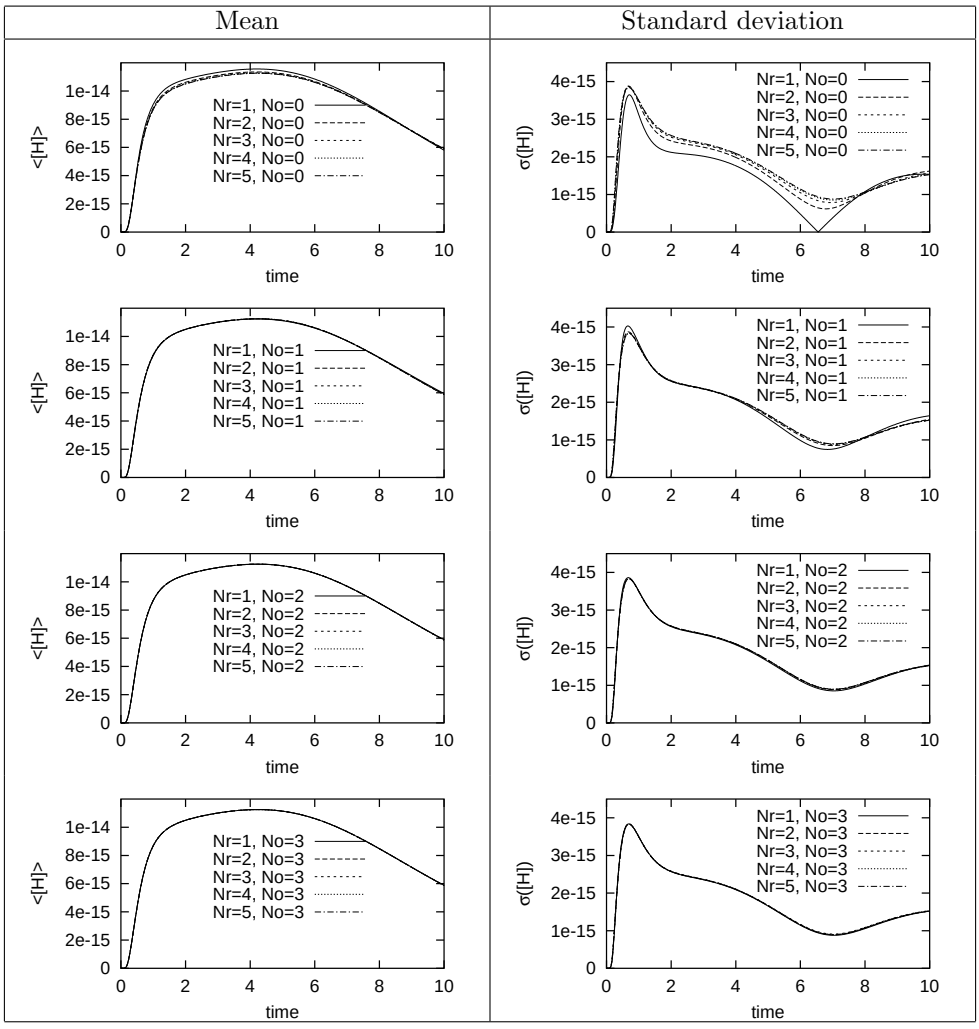

Figure 11: Mean (left) and standard deviation (right) of H concentration as a function of time. Computations with MW expansions using N_o and N_r as indicated. Only the uncertainty in the 7-th reaction (see Table 1) is considered, all other forward rates being taken equal to their median values.

To support this assertion, we show in the left plot of Figure 12 the time evolution of the expected concentration in H with the $\pm$ one standard deviation bounding box ($\sigma([\mathrm{H}])$). In addition, the deterministic solution corresponding to the median value of the forward rate (solid line) is also reported in the same plot. While one may have expected the deterministic median solution to remain roughly within the neighborhood of the expected solution, it appears that it actually departs significantly from the averaged realization, reaching the $+\sigma$ bound for $t \approx 6.5$. This behavior is characteristic of highly skewed processes, reflecting the non-linearity of the chemical source term. To better appreciate the skewness of the uncertainty in the H concentration distribution, we provide in the right plot of Figure 12 a set of 40 sample paths of $[\mathrm{H}](t)$ for random realizations of $\tilde{k}_{f,7}$ following the prescribed log-normal distribution. These sample paths highlight the complex dependence of the concentration on the actual value of the 7^{th} forward rate, and the clearly skewed distribution that results from it, with what appears as an upper limit in [H] for $t > 5$, that realizations are unlikely to cross. At this point, it should be clear that first- and second-order statistical moments are not enough to fully characterize the impact of the uncertainty in $k_{f,7}$ on the solution.

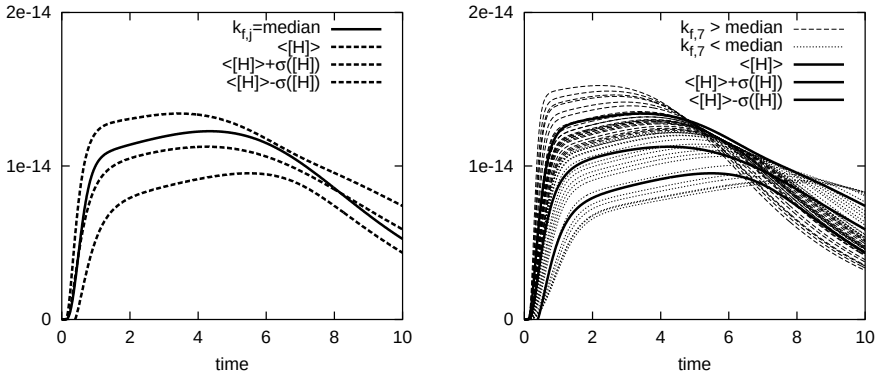

Figure 12: Left : mean of $[\mathrm{H}](t)$ with $\pm\sigma([H])$ box (dashed lines) and deterministic $[\mathrm{H}](t)$ for $\tilde{k}_{f,7}(x) = \hat{k}_{f,7}$ (solid line). Right : 40 deterministic samples of $[\mathrm{H}](t)$ (dashed lines) for random values of $\tilde{k}_{f,7}$ log-normally distributed, together with the computed expectation of $[\mathrm{H}](t) \pm \sigma([\mathrm{H}])$ (solid lines). Mean and standard deviation of $[\mathrm{H}](t)$ were obtained using $\mathrm{N_r} = 5$ and $\mathrm{N_o} = 3$.

5.3. Analysis of concentrations probability density functions

To stress further the need for accurate high order statistics in order to properly represent the impact of uncertainty on the chemical process under study, and to illustrate the improvement in this direction resulting from increasing the level of resolution in the MRA scheme, we now focus on the PDF of the species concentrations. To this end, we use for each species sp the time-dependent *relative likelihood* $\mathcal{R}_{[\mathsf{sp}]}$ of species concentration, defined as follows:

$$(\forall t \in [0,10]) \quad \mathcal{R}([\mathsf{sp}],t) = \frac{\mathrm{pdf}([\mathsf{sp}](t))}{\sup_{[\mathsf{sp}]} \mathrm{pdf}([\mathsf{sp}](t))}. \tag{38}$$

Hence, one always has $\mathcal{R}([\mathsf{sp}],t) \in [0,1]$, with equality to 1 if and only if $\mathrm{pdf}([\mathsf{sp}])$ is equal to the highest PDF at time t; this is in particular the case for the maximum likelihood estimation of $[\mathsf{sp}]$, when it exists – with no guarantee of unicity. On the contrary, $\mathcal{R}([\mathsf{sp}],t)$ vanishes if and only if the PDF of $[\mathsf{sp}]$ at time t vanishes as well. The rescaling of the concentration PDF, with its local-time maxima, enables time-tracking of the concentration value with the highest PDF, by removing the large fluctuations in magnitude of the absolute PDF. As with the PDF, however, a thin $\mathcal{R}$ for a given observable means a highly predictable concentration, while broad distributions or disperse peaks in $\mathcal{R}$ reflect large variability, possible unpredictability (at least unreliability) and a low confidence level in the predicted concentrations. In Figure 13, we have plotted the relative likelihood for two species concentrations: $[\mathrm{H_2}]$ and [H]. The PDFs of the species concentrations

were estimated using a set of one million samples for x, uniformly drawn on $[0, 1]$, and used to compute the corresponding concentration samples from their respective MW expansions.

The results in the figure clearly show the convergence of $\mathcal{R}([H_2], t)$ and $\mathcal{R}([H], t)$ (and so of their respective PDF) with increasing N_r. The dominant features of the $\mathcal{R}([H_2])$ time-evolutions are largely converged for $N_r = 3$, while low N_r artifacts in $\mathcal{R}([H], t)$ are not eliminated till $N_r = 4$ or 5. Further, while $\mathcal{R}([H_2], t)$ exhibits generally smooth behavior, persistent sharp features are evident in $\mathcal{R}([H], t)$ for $t > 4$. This suggests the role of implicit equilibrium constraints in the chemical system at late time (as equilibrium is approached), and the high sensitivity of the system to [H]. The result is that a very narrow distribution in [H] is allowed for $t > 4$. Of course it is true that $[H_2]$ also exhibits a narrowing distribution at late time, but of a clearly different qualitative nature. Note that the equilibrium state of the system is not uncertain, as it is determined by the thermodynamics of the mixture and not by the rate kinetics. Since uncertainty is only presumed here in the kinetic rate constant, it is expected that, for sufficiently large time, the residual distribution of $\mathcal{R}([H_2])$ and $\mathcal{R}([H])$ in the figure will approach peaked functions. Moreover, while $[H_2]$ tends to zero at equilibrium and must remain positive, [H] tends to a non-zero limit and is skewed towards an upper limit (highest concentrations).

5.4. Response-surfaces

Analogous to the response surface results shown in Figs 7-8 we examine here the MW response surfaces for the chemical system; specifically for [H], as function of time and $x(\xi)$. This data is shown in Figure 14 for $N_r \in \{1, 2, 3, 4\}$ and $N_o \in \{0, 1\}$, and in Figure 15 for $N_o \in \{0, 1, 2, 3\}$ and $N_r \in \{1, 2, 3\}$. The discrete jumps in the response surface for $N_o = 0$ are smoothed as N_o increases; these jumps are due to the discontinuous mapping of the reaction rate. The results indicate the general convergence of the representation of the response surface with increasing N_r and N_o. Moreover the change in the character of $\mathcal{R}([H])$ observed in Fig. 13 at late time is also evident here in the absence of any variation along the vertical axis in the [H] response surface at late time. This follows a significant growth in this variation at early time.

6. Multi-Dimensional Process

Direct extension of the methodology of the previous section to the full uncertain problem is not feasible, because the size of the MW basis, for given N_r and N_o exhibits a prohibitive rate of growth with the number of independent parameters. Also, if the uncertain process to be expanded is essentially smooth with regard to the parameter set, with only localized steep variations along only a few of the stochastic dimensions, one can expect that a large part of the MW coefficients have low magnitude, so that many can actually be neglected. However, the set of MW coefficients that could be removed from the expansion is not known a priori, and an adaptive strategy that dynamically selects the relevant coefficients is required in order to maintain an acceptable computational cost.

Although appealing, adaptive strategies based on coarsening/refinement of the set of MW coefficients is difficult to implement in multi-dimensional problems, and not necessarily optimal from a CPU-load point of view, since any changes in the basis imply changes in the product tensors D_{ijk}, whose evaluation can be expensive if it were to be repeated many times during the simulation. Further, when the number of MW coefficients increases, the size of the set of non-vanishing elements in the binary and ternary products increases dramatically (see [13]) due to the overlapping supports of the MW at different resolution levels. This is a severe limitation for the use of MW expansions for $N_d > 1$ because the binary product is the key operator in pseudo-spectral computations [8, 17].

These considerations lead us to the development of an alternative adaptive strategy in [13], which retains the fundamental feature of MRA, specifically the piecewise polynomial character of the expansion, while overcoming the issue of increasing complexity of the binary product when the resolution level increases. The main ingredient of this adaptive scheme is the construction of an "analyzer-basis", involving multidimensional Legendre polynomials plus first resolution level one-dimensional details. This analyzer can be rescaled (to an arbitrary resolution level in each of the stochastic dimensions) and displaced (within the parameter space) to compute local expansions of the process. Within this framework, the aim of the adaptive strategy is to

decide what is the minimal local level of resolution necessary to properly approximate the solution. Below, we detail the construction of the adaptive scheme, which is then applied to the chemical test-problem.

6.1. Set Partition of the Parameter Space and Local Basis

We now develop a local refinement scheme based on the expansion in Eq. (16). Comparison of the two expansions in Eqs. (16) and (17) shows that the former, in terms of ϕ functions, does not involve any summation over the scale indices, contrary to the expansion in terms of details, ψ. This difference stems from the fact that the basis functions ϕ_{il}^k, $i = 0, \ldots, N_o$ and $l = 0, \ldots, 2^k - 1$, couple with only N_o other components, namely those having the same sliding index l. In contrast, the ψ_{il}^k couple with many other components. This suggests an adaptive strategy based on successive set partitions of the random parameter space, through the determination of a local resolution level. Let $\Omega = [a_1, b_1] \times \cdots \times [a_N, b_{\mathrm{N_d}}]$ be space of random parameters. Let Ω^m, $m = 1, \ldots, \mathrm{N_b}$ be a finite set partition of Ω in $\mathrm{N_b}$ non-overlapping sub-domains:

$$\begin{cases} \Omega^m = [a_1^m, b_1^m] \times \ldots [a_N^m, b_N^m], \\ \Omega = \bigcup_{m=1}^{\mathrm{N_b}} \Omega^m, \\ \Omega^m \cap \Omega^{m'} = \varnothing \quad \text{if } m \neq m'. \end{cases} \tag{39}$$

We define as follows the local probability density function of $\boldsymbol{\xi}$ on each of the sub-domains Ω^m, denoted by $\mathrm{pdf}^m(\boldsymbol{\xi})$, using the independence of the random parameters:

$$\mathrm{pdf}^m(\boldsymbol{\xi}) = \prod_{d=1}^{\mathrm{N_d}} \mathrm{pdf}_d^m(\xi_d), \quad \mathrm{pdf}_d^m(\xi) = \frac{\mathrm{pdf}_d(\xi)}{\mathrm{p}_d(b_d^m) - \mathrm{p}_d(a_d^m)}. \tag{40}$$

Clearly, we have

$$\mathrm{pdf}^m(\boldsymbol{\xi}) > 0 \quad \text{for } \boldsymbol{\xi} \in \Omega^m \text{ and } \int_{\Omega^m} \mathrm{pdf}^m(\boldsymbol{\xi}) d\boldsymbol{\xi} = 1. \tag{41}$$

Moreover, defining

$$\mathrm{p}_d^m(\xi \in [a_d^m, b_d^m]) = \int_{a_d^m}^{\xi} \mathrm{pdf}_d^m(\xi') d\xi' \in [0, 1], \tag{42}$$

if x_d^m is uniformly distributed over $[0, 1]$, then the random variable $(\mathrm{p}_d^m)^{-1}(x_d^m) \in [a_b^m, b_d^m]$ and has the same distribution as ξ_d^m. Thus, a second-order stochastic process can be locally expanded on Ω^m, in terms of the random vector $\boldsymbol{x}^m$, having independent components $(x_1^m, \ldots, x_{\mathrm{N_d}}^m) \in [0, 1]^{\mathrm{N_d}}$, with uniform distributions. Now let $\boldsymbol{\gamma}$ be the set of multidimensional indices

$$\boldsymbol{\gamma}(\mathrm{N_o}) = \left\{ (\gamma_1, \ldots, \gamma_{\mathrm{N_d}}) : \sum_{d=1}^{\mathrm{N_d}} \gamma_d \leq \mathrm{N_o} \right\}.$$

For $\boldsymbol{\xi} \in \Omega^m$, we build the local projection basis as

$$\mathcal{B}_p(\Omega^m, \mathrm{N_o}) = \left\{ \Phi^m_{\boldsymbol{\lambda} \in \boldsymbol{\gamma}(\mathrm{N_o})}(\boldsymbol{x}^m(\boldsymbol{\xi}^m))) = \prod_{d=1}^{\mathrm{N_d}} \phi_{\lambda_d}(x_d^m(\xi_d^m)) \right\},$$

and the details directional basis $\mathcal{B}_a^d(\mathrm{N_o})$, $d = 1, \ldots, \mathrm{N_d}$ as

$$\mathcal{B}_a^d(\Omega^m, \mathrm{N_o}) = \{\psi_i(x_d^m), i = 0, \ldots, \mathrm{N_o}\}.$$

The full local expansion basis will be the union of $\mathcal{B}_p$ and $\mathcal{B}_a^d$:

$$\mathcal{B}(\Omega^m, \mathrm{N_o}) = \mathcal{B}_p(\Omega^m, \mathrm{N_o}) + \bigcup_{d=1}^{\mathrm{N_d}} \mathcal{B}_a^d(\Omega^m, \mathrm{N_o}).$$

Finally, the multidimensional process $\mathcal{P}(\boldsymbol{\xi})$ will have for local expansion on Ω^m:

$$\mathcal{P}(\boldsymbol{\xi}) = \tilde{\mathcal{P}}(\boldsymbol{x}^m(\boldsymbol{\xi})) \approx \sum_{\boldsymbol{\lambda}\in\boldsymbol{\gamma}} \tilde{\mathcal{P}}^m_{\lambda_1,\ldots,\lambda_N} \Phi_{\lambda_1,\ldots,\lambda_N}(\boldsymbol{x}^m(\boldsymbol{\xi})) + \sum_{d=1}^{\mathrm{N_d}} \sum_{i=0}^{\mathrm{N_o}} \tilde{\mathcal{P}}^m_{d,i} \psi_i(x^m_d), \tag{43}$$

where again, the equality holds in the mean-square sense.

Note that the local basis $\mathcal{B}(\Omega^m, \mathrm{N_o})$, spanning the local expansion of $\mathcal{P}$ according to Eq. (43), is in fact the rescaled Legendre polynomials basis ($\mathcal{B}_p(\Omega^m, \mathrm{N_o})$) augmented with the first-level detail basis, $\mathcal{B}^d_a$, $d = 1, \ldots, \mathrm{N_d}$. Thus, $\tilde{\mathcal{P}}(\boldsymbol{x})$, for $\boldsymbol{\xi}(\boldsymbol{x}) \in \Omega^m$, approximated by Eq. (43) is the local Wiener-Legendre projection of order $\mathrm{N_o}$, plus one dimensional details. The local expectation of $\mathcal{P}$ is given by $\langle\mathcal{P}\rangle_{\Omega^m} = \mathcal{P}^m_{0,\ldots,0}$, and its local variance is

$$\sigma^2_{\Omega^m}(\mathcal{P}) \approx \left(\hat{\sigma}_{\Omega^m}\right)^2 + \sum_{d=1}^{\mathrm{N_d}} \left(\sigma^d_{\Omega^m}\right)^2,$$

where $\left(\hat{\sigma}_{\Omega^m}\right)^2 = \sum_{\boldsymbol{\lambda}\in\boldsymbol{\gamma}_p} (\mathcal{P}^m_{\boldsymbol{\lambda}})^2$, $\left(\sigma^d_{\Omega^m}\right)^2 = \sum_{i=0}^{\mathrm{N_o}} \left(\mathcal{P}^m_{d,i}\right)^2$, and we have denoted $\boldsymbol{\gamma}_p = \boldsymbol{\gamma} - \{(0,\ldots,0)\}$. The total expectation of the process is given by the volume-weighted summation of the local expectations:

$$\langle\mathcal{P}\rangle = \sum_{m=1}^{\mathrm{N_b}} \langle\mathcal{P}\rangle_{\Omega^m} \mathrm{Vol}^m, \tag{44}$$

where Vol^m is the Euclidean volume of Ω^m: $\mathrm{Vol}^m = \prod_{d=1}^{\mathrm{N_d}} (\mathrm{p}_d(b^m_d) - \mathrm{p}_d(a^m_d))$. Finally the total variance of the process is given by

$$\sigma^2(\mathcal{P}) = \sum_{m=1}^{\mathrm{N_b}} \left[\sigma^2_{\Omega^m}(\mathcal{P}) + \left(\mathcal{P}^m_{0,\ldots,0} - \langle\mathcal{P}\rangle\right)^2\right] \mathrm{Vol}^m. \tag{45}$$

6.1.1. Adaptive strategy

Assume that the current set partition of Ω involves $\mathrm{N_b}$ blocks, *i.e.* $\Omega = \bigcup_{m=1}^{\mathrm{N_b}} \Omega^m$. On each sub-domain Ω^m, the process is expanded on the local basis $\mathcal{B}(\Omega^m, \mathrm{N_o})$, the spectral coefficients being computed through Galerkin projection methods as previously. To decide if a given block m needs more refinement, and to determine which stochastic directions need such refinement, we consider the following criterion:

$$C_m(d) = \frac{\sigma^d_{\Omega_m}}{\sigma_{\Omega_m}} \geq \varepsilon_r \tag{46}$$

and we refine the sub-domain along the d-th dimension if this inequality is satisfied. Here $\varepsilon_r < 1$ is a prescribed threshold function. The test compares the "energy" of the one-dimensional details along the d-th stochastic direction with the local variance of the solution. In other words, the one-dimensional details coefficients are used as indicators of the quality of the representation along their respective stochastic direction. A new set partition of Ω is then constructed, by splitting Ω^m into smaller sub-domains. Specifically, if we assume the inequality (46) is satisfied for a single dimension d, then refinement of $\Omega^m = [a^m_1, b^m_1] \times \cdots \times [a^m_N, b^m_N]$ will give birth to two new sub-domains $\Omega^{m'}$ and $\Omega^{m''}$, defined by:

$$\begin{cases} \Omega^{m'} & = [a^{m'}_1, b^{m'}_1] \times \cdots \times [a^{m'}_N, b^{m'}_N] \\ & = [a^m_1, b^m_1] \times \cdots \times [a^m_d, (a^m_d + b^m_d)/2] \times \cdots \times [a^m_N, b^m_N] \\ \Omega^{m''} & = [a^{m''}_1, b^{m''}_1] \times \cdots \times [a^{m''}_N, b^{m''}_N] \\ & = [a^m_1, b^m_1] \times \cdots \times [(a^m_d + b^m_d)/2, b^m_d] \times \cdots \times [a^m_N, b^m_N]. \end{cases} \tag{47}$$

Then, local expansions of the process on the newly created sub-domains are computed, before being analyzed to determine whether additional refinement is needed. This sequence of analysis and refinement steps is repeated up to convergence. It is emphasized that, during refinement, computations are performed in newly created sub-domains only, since the local solutions over other sub-domains are unaffected. Note also that this methodology is well suited for parallel implementation, since local computations are independent of each other.

6.1.2. Application to chemical systems

We now provide the algorithm used to integrate the system of stochastic ODEs governing the uncertain supercritical hydrogen oxidation mechanism, with dynamical adaptation of the parameter space set partition. In order to minimize the computational load, we do not recompute the solution, starting from the initial time, for each refined sub-domain, as in [13]. Instead, we advance the solution in time using equally spaced stages, where the correctness of the set partition with regard to the threshold function ϵ_r is verified. If the set partition at the end of a given stage k needs further refinement, then it is refined, and the solution over the created sub-domains is computed from the initial conditions corresponding to the solution at the end of the stage $k-1$. A procedure is required to provide initial conditions for the new sub-domains at the beginning of the current stage k. This is performed efficiently and without approximation using polynomial interpolations of the solution of the "parent" sub-domain that has been split.

Suppose that we wish to integrate the system for $t \in [0, T_f]$. We denote ΔT the time-interval between successive analyses of the set partition. With this notation, the time-marching algorithm has the following structure:

1. **Initialization:**
   (a) set times $t = 0$, $t_0 = 0$ and $t' = \Delta T$;
   (b) Initialize the set partition of Ω to $\Omega^1 = [0,1]^{\mathrm{N_d}}$, $\mathrm{N_b} = 1$.
   (c) Project the initial condition of the concentration on Ω^1.
   (d) Set sub-domain flag $I(m = 1)$ to 1.
2. For each sub-domain Ω^m of the set partition, $m = 1, \ldots, \mathrm{N_b}$ with $I(m) = 1$:
   (a) Set the local expansion of the forward and reverse reaction rates;
   (b) Set the local expansions for the concentrations at time t_0;
   (c) Perform the time integration between t_0 and t' of the local system of stochastic ODEs;
3. Set $\mathrm{N_b}' = \mathrm{N_b}$.
4. For each sub-domain Ω^m of the set partition, $m = 1, \ldots, \mathrm{N_b}'$, with flag $I(m) = 1$:
   (a) Set sub-domain flag to $I(m) = 2$;
   (b) Compute $C_m(d)$ given by Eq.(46), and retain highest value over the set of species concentrations;
   (c) If $\forall d = 1, \ldots, \mathrm{N_d}$: $C_m(d) < \varepsilon_r$, then do:
      i. The sub-domain is sufficiently refined, update flag to $I(m) = 0$;
      ii. Continue with the next sub-domain in the list (step number (4)).
   (d) Else, for $d = 1, \ldots, \mathrm{N_d}$ do:
   If $C_m(d) \geq \varepsilon_r$ then do:
      i. For every sub-domain $\Omega^{m' \leq \mathrm{N_b}}$ with $I(m') = 2$, do:
         - Store the solution S_0 at time t_0 over $\Omega^{m'}$;
         - Split (along the d-dimension) the sub-domain $\Omega^{m'}$ into two sub-domains with index m' and $m'' = \mathrm{N_b} + 1$: $\Omega^{m'} \rightarrow \Omega^{m'} \cup \Omega^{m''}$;
         - Set $I(m')$ and $I(m'')$ to 3 to make sure they are refined only once;
         - Interpolate S_0 on $\Omega^{m'}$ and $\Omega^{m''}$;
         - Update the set partition: $\mathrm{N_b} \leftarrow \mathrm{N_b} + 1$.
      ii. Shift all sub-domain flags with value 3 to $I = 2$, and proceed with the next dimension d in step (d).
   (e) Refinement of the sub-domain has been completed, set all flags $I = 2$ to $I = 1$ and proceed with the next sub-domain in step (4).
5. If $\mathrm{N_b} > \mathrm{N_b}'$, new sub-domains have been generated that need to be computed and further analyzed: continue from step (2).
6. The set partition satisfies the refinement criteria, then:
   (a) Record the set partition and the solutions over all sub-domains at time $t = t'$, to be used as initial conditions in the next time interval;
   (b) If $t' < T_f$, then:
      i. Set $t_0 \leftarrow t'$, $t' \leftarrow t' + \Delta T$;
      ii. For $m = 1, \ldots, \mathrm{N_b}$ set $I(m) = 1$;
      iii. Continue from step (2).
7. End.

6.2. Test cases

We now present some test cases in order to illustrate the validity of our approach.

6.2.1. 2-dimensional tests

We consider uncertainty in the rates of reactions 7 and 8, and apply the adaptive scheme for three threshold values $\epsilon_r = 0.025$, 0.01 and 0.001. Tests are considered for the first and second order expansion.

In Figure 16, we plot the final ($t = 10$) set partitions, response-surfaces together with the time evolutions of the number of block in the set partition, for the six tests. The results highlight the dependence of the MW discretization and domain decomposition on ϵ_r and $\mathrm{N_o}$. The top panel shows the partitioning of the (x_7, x_8) plane, and its dependence on ϵ_r and $\mathrm{N_o}$. We note the more refined partitioning with decreasing ϵ_r and $\mathrm{N_o}$.

For higher $\mathrm{N_o}$, less refinement of the (x_7, x_8) space is necessary for a given allowed directional block variance, controlled by ϵ_r. The localization of the highly refined domain blocks at the $(0, 1)$ limits of x_7 and x_8 reflect both the variability of the rate constant mappings (as shown in Fig. 9) and the dependence of various elements of the solution on the (x_7, x_8) space. The dependence of [H] (at $t = 10$) on (x_7, x_8) is shown in the middle panel in Fig. 16, again for the indicated ranges of ϵ_r and $\mathrm{N_o}$. The [H] response surfaces exhibit strong variability with (x_7, x_8) in the vicinity of the origin, with generally smoother behavior elsewhere. Sensitivity information can be conveniently extracted from the response surfaces.

Finally the bottom panel in the figure shows the time evolution of the number of bins N_b for the indicated ranges of ϵ_r and $\mathrm{N_o}$. In all cases, results indicate fast initial growth of the number of bins as the ignition process unfolds, till about $t = 2$. Past this time, N_b increases only slightly, if any, as the system approaches equilibrium, and the solution becomes gradually more insensitive to uncertainties in the rate constants.

The results clearly suggest the need for a coarsening strategy to accelerate the solution at late time, as it is expected that many of the bins created at early time are no longer necessary as the system approaches equilibrium at late time. The N_b-profiles also show clearly the need for higher N_b when both ϵ_r and $\mathrm{N_o}$ are low, as observed pictorially in the top and middle panels in the figure. An optimal strategy ultimately requires suitable choices of $\mathrm{N_o}$ and ϵ_r for the problem at hand.

We note finally the relative insensitivity of the [H] response surface shape to the choice of ϵ_r and $\mathrm{N_o}$ in the ranges considered in Fig. 16. This is also evident in the mean and standard deviation profiles of [H] versus time shown in Fig. 17. Any changes in these two moments over the specified range of ϵ_r and $\mathrm{N_o}$ is simply not observable in the profiles for all time.

6.2.2. High dimensional tests

In this section the adaptive scheme is again applied considering all the reaction rates as uncertain. The simulation runs up to $t = 10$ as previously. Figure 18 displays the numbers of bins involved in the partitions as a function of time, for different orders $\mathrm{N_o}$ and refinement threshold ϵ_r. As for the previous case, Figure 18 indicates that the number of bins quickly increases at the early stages of the simulation and then tends to level off. It may also be noticed that with $\epsilon_r = 0.05$ and $\mathrm{N_o} = 3$ the computations do not reach $t = 10$ because of numerical instabilities (even though the computations are stable for a longer period than with WHe expansions).

Clearly, the efficiency of the partitioning strategy depends on the capability of the algorithm to divide the parameter space into an optimal number of sub-domains. To minimize this number of sub-domains, the successive divisions have to be limited to the directions along which steep dependences are present, while avoiding division along smooth dimensions. To appreciate the capability of the algorithm to discriminate directions (uncertain reaction rates) requiring divisions from the smooth ones, we present in Figure 19 the frequency of successive divisions along the different dimensions of the parameter space for $\mathrm{N_o} = 1$ and two threshold values. For $\epsilon_r = 0.05$ it is shown that no division is generated along dimensions 1-4 and 6, denoting a smooth dependence of the concentrations with regard to the uncertainties in the corresponding reaction rates. On the contrary, reactions 5, 7 and 8 do require divisions, up to 3 successive ones in some areas of the parameter space. When ϵ_r is lowered to 0.005, more divisions are necessary along the previously divided directions, to meet the refinement criteria, while some sub-domains have now also been cut along directions 6 and 2, but with a significantly lower frequency.

It has been reported that using a larger expansion order requires a lower number of sub-domains to satisfy a fixed refinement criteria. However, the dimension of the local basis quickly increases with the order N_o such that a lower number of sub-domains does not necessarily imply a lower computational cost. In fact, for given ϵ_r, the selection of the optimal order in terms of CPU cost remains an open question. Moreover, because the solutions over sub-domains are fully independent and can be computed in parallel, the trade-off between number of sub-domains and expansion order should account for memory requirement and data flow as well. Also, the optimal trade-off is certainly problem dependent so no general guidelines can be established. Another aspect that needs to be underlined is that different orders used with the same threshold value will not generally leads exactly to the same accuracy, although the same order of error is expected. To verify this assertion, we provide in Figure 20 the time-evolutions of the standard deviations in [H] and [OH] when computed with $N_o = 1$ and $N_o = 2$ and for two threshold values $\epsilon_r = 0.05$ and 0.01. It is observed that all the predictions are in good agreement and appears to converge to the most refined and highest order solution. Similar conclusions are obtained from the analysis of other concentrations and the analysis of their expectations. In fact, for $\epsilon_r = 0.005$ and $N_o = 1$, the predictions are not distinguishable from the case $N_o = 2$, $\epsilon_r = 0.01$ (not shown).

Again, Figure 20 suggests a fast convergence of the solution with both the threshold value and the expansion order. However, if one is interested in a more complete statistical description of the solution, then the improvement in the prediction with decreasing ϵ_r and increasing expansion order are more visible. To illustrate this fact, we provide a quick analysis of the resulting pdfs of some species concentrations. Provided in Figure 21 are pdfs of [H], [H_2], [HO_2] and [H_2O_2] at different times, computed with $N_o = 1$ and $\epsilon_r = 0.005$. The plots indicate that the pdfs are smooth (except at the tails) denoting no significant discontinuities of the solution across sub-domain boundaries. For lower refinement thresholds ($\epsilon_r = 0.1$) discontinuities are present (not shown). Also, the plots demonstrate the need for an adaptation of the partition, as the shape of the pdfs drastically evolve with time. It is clear that such a complex uncertainty impact would have required a large order expansion if a global expansion is to be used (*i.e.* only one domain), but such high order global expansion is numerically unstable as shown in [17].

Finally, the numerical instabilities in the global spectral simulations reported in [17] were attributed to the spurious development of tails with negative concentrations in the solution expansion. Although the present computations are stable, it is interesting to note that our simulations does not totally satisfy the positivity of the concentrations: the probability of all concentration being positive is not exactly 0. This is illustrated in Figure 22 where pdfs of [H] is plotted at time $t = 10$ for different orders and threshold values. These plots show that the probability of [H] < 0 decreases with the order and the refinement criteria (similar behavior is observed for the other species). It can be concluded that the automatic partitioning of the parameter space stabilized the computation by maintaining a low order expansion, valid locally, and dividing a sub-domain whenever its local solution develops instability. This effect is further illustrated in Figure 23, which compares the computed pdfs of [H] at $t = 10$ for a fixed order $N_o = 1$ and different refinement criteria.

7. Conclusions

In this paper, a Multi-Resolution Analysis scheme for the quantification of parametric uncertainties in chemical systems has been developed. The impact of uncertainties is tackled using an orthogonal projection of the model solution on spectral bases made of piecewise continuous polynomial functions (Multi-Wavelets) of a set of random variables, which represents the variability in the system parameters. This approach is a generalization of the classical global Polynomial Chaos expansions and is designed to allow for local refinement of the representation in areas of the uncertain parameter space where it is needed. Such local refinements are required when the system dynamics exhibits complex and steep dependences with regard to the random parameters (here the reaction rates), a situation which is commonly encountered in chemical systems. In fact, instead of using unnecessary large order global PC expansions a series of local low order expansions at controlled resolution levels are employed.

The main improvement of the proposed MRA scheme comes from the numerical instability of the computational methods (Galerkin projection) for the determination of the expansion coefficients, when the

expansion order increases. Thus, maintaining a low to moderate expansion order is crucial for the robustness of the computations, while convergence can still be controlled through the selection of an appropriate level of resolution. Even-though the improvement of the computational stability allowed us to obtain accurate predictions for simple problems, where global expansions were challenged, the fast increase of the basis dimension with the resolution level prevents the straightforward application of the MRA scheme to situations involving multiple independent random parameters, and calls for adaptive techniques. Consequently, a first attempt toward the local adaptation of the resolution level is proposed. This adaptive technique makes use of the energy contained in the local correction at the next resolution level to decide if more resolution is needed. It naturally leads to an iterative partition of the parameter space, up to a prescribed tolerance, with the property that its computational cost is proportional to the resulting number of subdomains in the partition and not a function of the basis dimension. Numerical experiments have demonstrated the validity of the proposed adaptive scheme, but also highlight the need for an improvement of the methodology to include a coarsening strategy and ultimately a local adaptation of the expansion order too. In fact, the optimal trade-off, between refinement of the partition into smaller subdomains and/or an increase of the local expansion order, to reduce the approximation error is problem dependent and need further investigations; a possible way to determine such optimal strategy could be based on *a posteriori* error estimators. Future developments will focus on this aspect.

References

[1] M. Abramowitz and I.A. Stegun. *Handbook of Mathematical Functions*. Dover, 1970.

[2] B. Alpert, G. Beylkin, D. Gines, and L. Vozovoi. Adaptive solution of partial differential equations in multiwavelet bases. *Journal of Computational Physics*, 182:149–190, 2002.

[3] B.K. Alpert. A class of bases in L_2 for the sparse representation of integral operators. *SIAM J. Math. Anal.*, 24:246–262, 1993.

[4] P.N. Brown, G.D. Byrne, and A.C. Hindmarsh. VODE : A variable coefficient ODE solver. *SIAM J. Sci. Stat. Comput.*, 10:1038–1051, 1989.

[5] G.D. Byrne and A.C. Hindmarsh. A polyalgorithm for the numerical solution of ordinary differential equations. *ACM Trans. Math. Software*, 1:71–96, 1975.

[6] R.H. Cameron and W.T. Martin. The orthogonal development of nonlinear functionals in series of fourier-hermite functionals. *Ann. Math.*, (48):385–392, 1947.

[7] B. Debusschere, H. Najm, A. Matta, R. Ghanem, and O. Le Maître. Protein labeling reactions in electrochemical flow : Numerical simulation and uncertainty propagation. *Physics of Fluids*, 15(8):2238–2250, 2003.

[8] B. Debusschere, H. Najm, P. Pébay, O. Knio, R. Ghanem, and O.P. Le Maître. Numerical challenges in the use of Polynomial Chaos representations for stochastic processes. *SIAM J. Sci. Comput.*, 26(2):698–719, 2004.

[9] R. Ghanem. The nonlinear gaussian spectrum of lognormal stochastic processes and variables. *ASME J. App. Mech.*, 66:964–973, 1999.

[10] R.G. Ghanem and P.D. Spanos. *Stochastic Finite Elements: A Spectral Approach*. Springer Verlag, 1991.

[11] M. Grigoriu. *Stochastic Calculus, Applications in Sciences and Engineering*. Birkhäuser, 2002.

[12] O.P. Le Maître, O.M. Knio, H.M. Najm, and R.G. Ghanem. Wiener-Haar expansion of stochastic processes. *J. Comp. Phys.*, 197(2):28–57, 2004.

[13] O.P. Le Maître, H.M. Najm, R.G. Ghanem, and O.M. Knio. Multi-resolution analysis of Wiener-type uncertainty propagation schemes. *J. Comp. Phys.*, 197(2):502–531, 2004.

[14] J.S. Liu. *Monte Carlo Strategies in Scientific Computing*. Springer Verlag, 2001.

[15] O.P. Le Maître, M.T. Reagan, O.M. Knio, H.N. Najm, and R.G. Ghanem. A stochastic projection method for fluid flow. ii. random process. *J. Comp. Phys.*, 181(1):9–44, 2002.

[16] B.D. Phenix, J.L. Dinaro, M.A. Tatang, J.W. Tester, J.B. Howard, and G.J. McRae. Incorporation of Parametric Uncertainty into Complex Kinetic Mechanisms: Application to Hydrogen Oxidation in Supercritical Water. *Combustion and Flame*, 112:132–146, 1998.

[17] M.T. Reagan, H.N. Najm, B.J. Debusschere, O.P.Le Maître, O.M. Knio, and R.G. Ghanem. Spectral stochastic uncertainty quantification in chemical systems. *Combustion Theory and Modelling*, 8:607–632, 2004.

[18] M.T. Reagan, H.N. Najm, R.G. Ghanem, and O.M. Knio. Uncertainty quantification in reacting flow simulations through non-intrusive spectral projection. *Combustion and Flame*, 132:545–555, 2003.

[19] S. Wiener. The homogeneous chaos. *Amer. J. Math.*, 60:897–936, 1938.

[20] D.B. Xiu and G.E. Karniadakis. The Wiener-Askey Polynomial Chaos for stochastic differential equations. *SIAM J. Sci. Comput.*, 24:619–644, 2002.

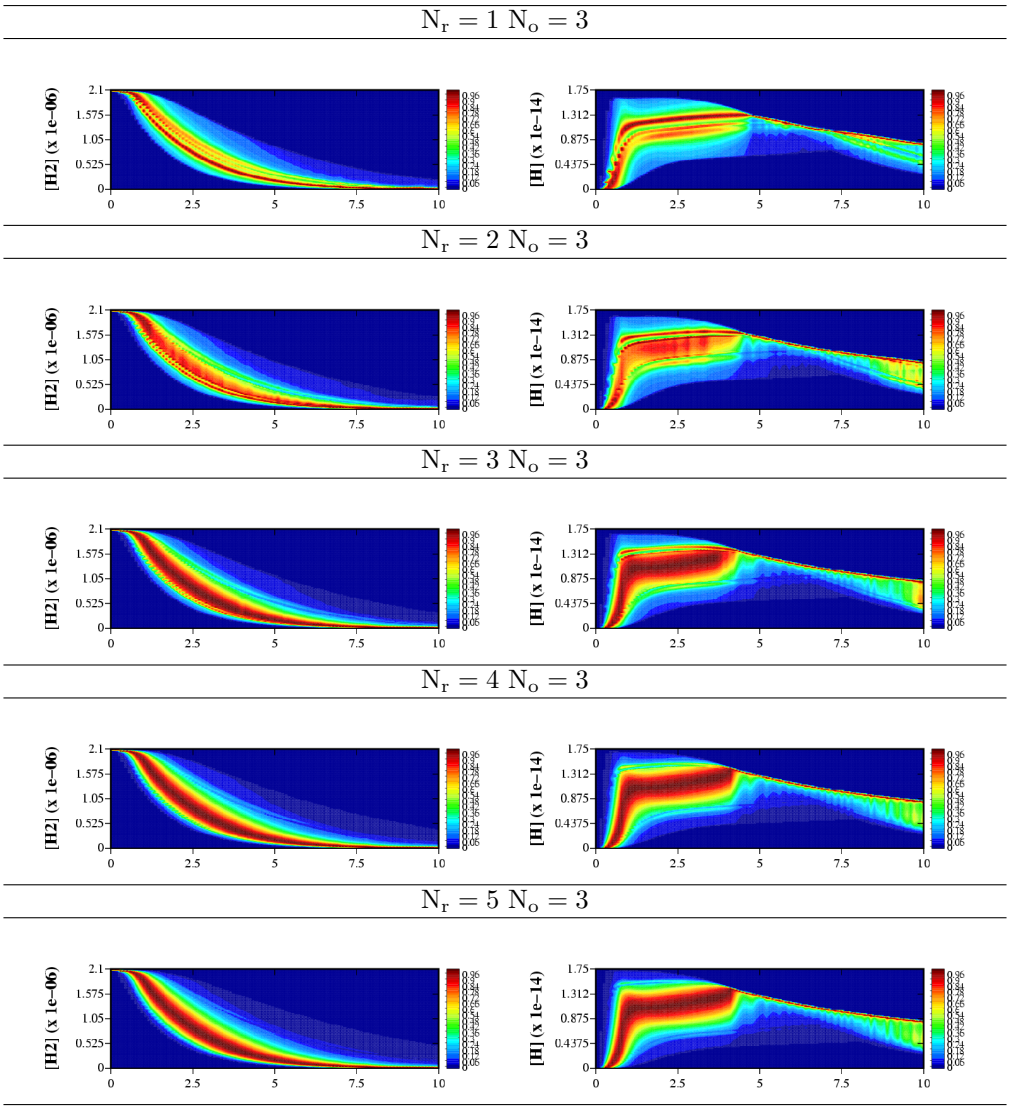

Figure 13: Color coded normalized probability density functions $\mathcal{R}([\mathrm{H}_2], t)$ (left) and $\mathcal{R}([\mathrm{H}], t)$ (right) computed from their MW expansion using different levels of resolution as indicated, and polynomial order $\mathrm{N_o} = 3$. Dark red areas indicate concentrations of highest probability density of observation, while deep blue regions correspond to vanishing probability densities.

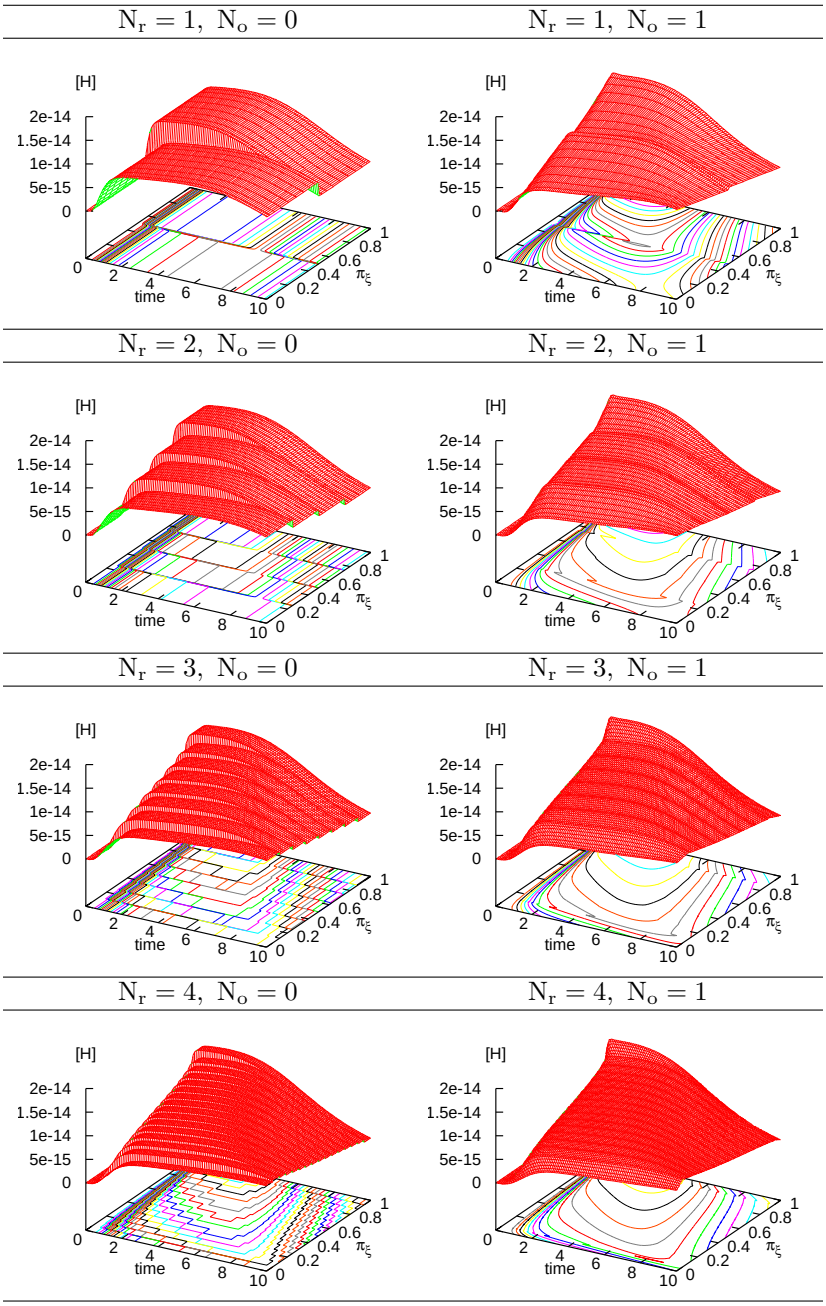

Figure 14: Response-surface for the concentration in H as a function of time and $x(\xi)$, for the 7-th reaction uncertain only. Surfaces are generated using zero order (left) and first order (right) MW expansions, with increasing level of resolution as indicated.

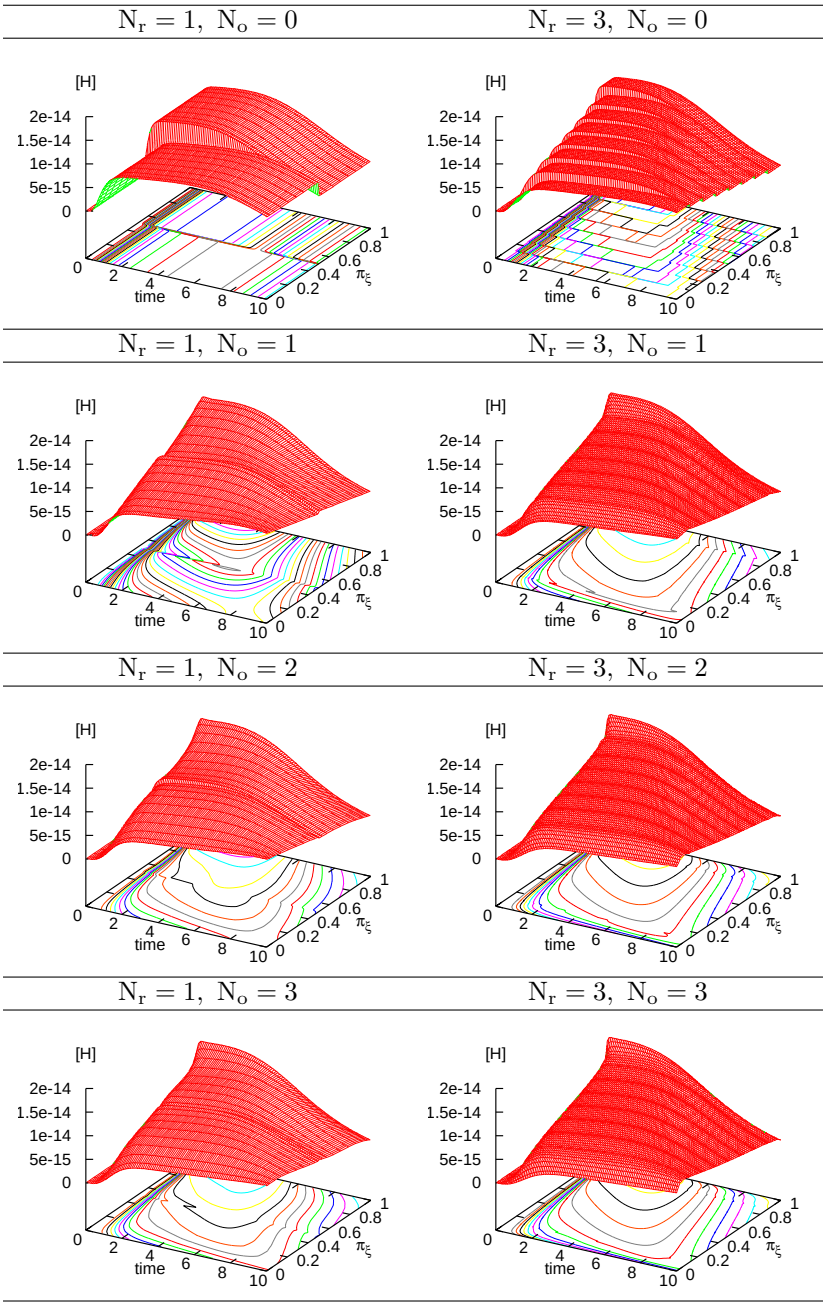

Figure 15: Response-surface for the concentration in H as a function of time and $x(\xi)$, for the 7-th reaction uncertain only. Surfaces are generated using one (left) and three (right) levels of resolution, and $N_o = 0, \ldots 3$ as indicated.

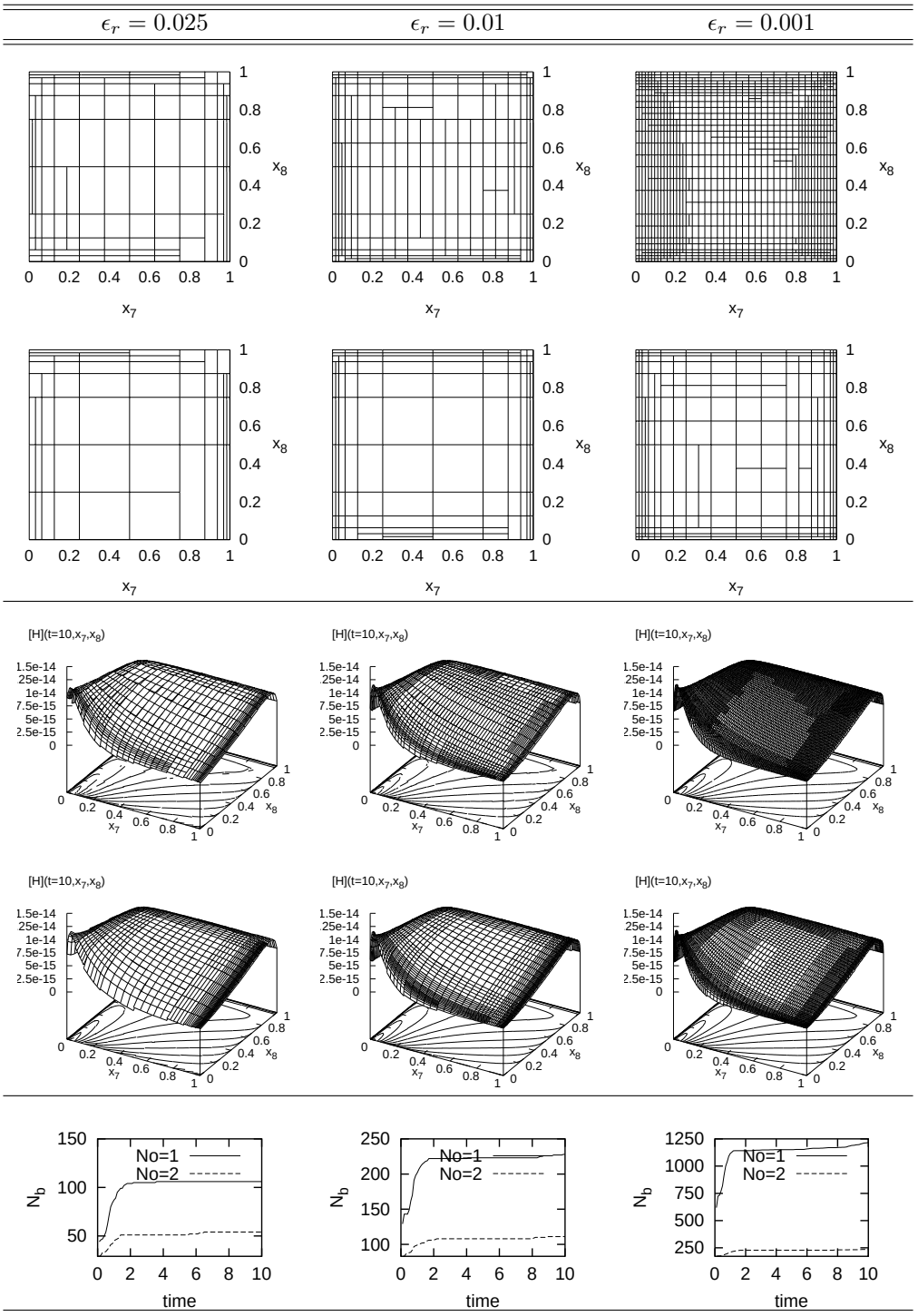

Figure 16: Results for the 2D problem considering uncertainty in the rates of reactions 7 and 8. Each column of plots corresponds to a given value of ϵ_r, with $\epsilon_r = 0.025, 0.01, 0.001$ from left to right. The top first and second rows of plots are for $\mathrm{N_o} = 1, 2$ respectively. Similarly for the next two rows. The top panel shows the partitioning of the (x_7, x_8) plane and its dependence on ϵ_r and $\mathrm{N_o}$. The middle panel shows the dependence of the [H] at $t = 10$ on x_7 and x_8. The bottom panel in the figure shows the time evolution of the number of bins N_b for the indicated ranges of ϵ_r and $\mathrm{N_o}$.

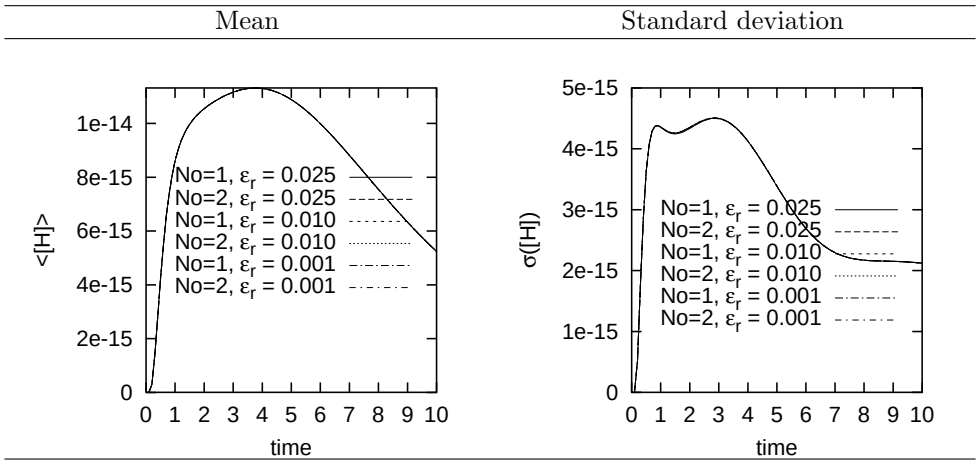

Figure 17: 2D-problem for uncertain reaction-rates of reactions 7 & 8. The left frame shows the dependence of the mean [H] time evolution on ϵ_r and N_o. The right frame shows similar information for the standard deviation of [H].

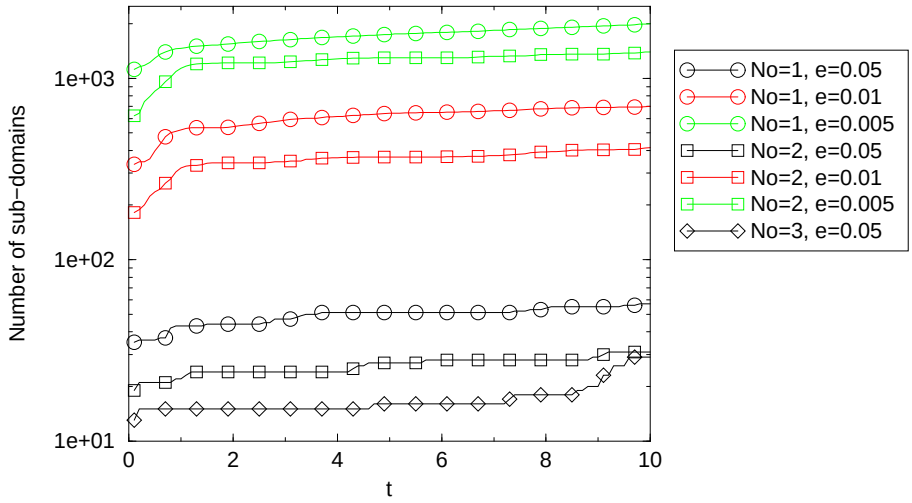

Figure 18: Evolution of the number of bins in the partitions as a function of time and for different expansion orders N_o and refinement threshold value ϵ_r as indicated.

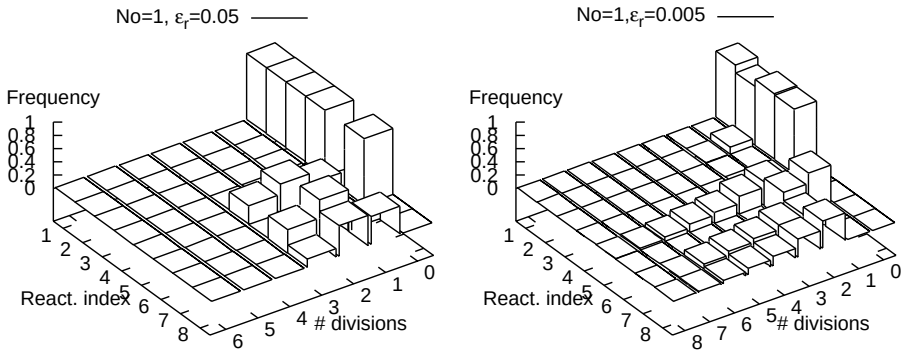

Figure 19: Relative frequency along each dimension of the parameter space (Reaction indices) of the number of successive divisions. The graphs correspond to the partition at time $t = 10$, for $N_o = 1$ and two threshold values $\epsilon_r = 0.05$ and 0.005.

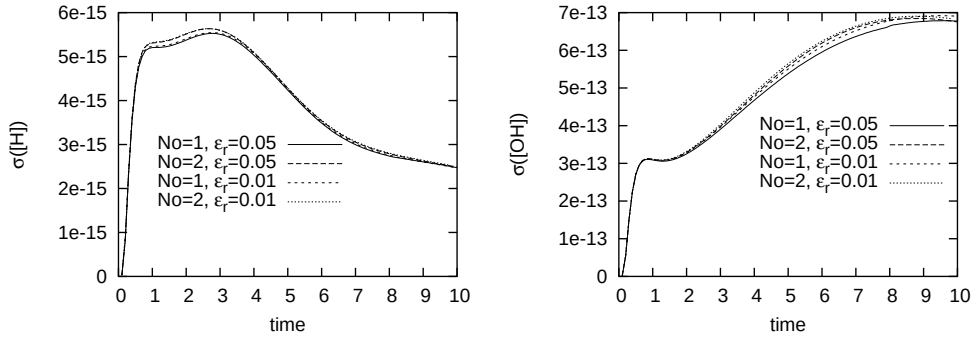

Figure 20: Computed standard deviations in [H] and [OH] as a function of time, for $N_o = 1$, 2 and $\epsilon_r = 0.05$ and 0.01 as indicated.

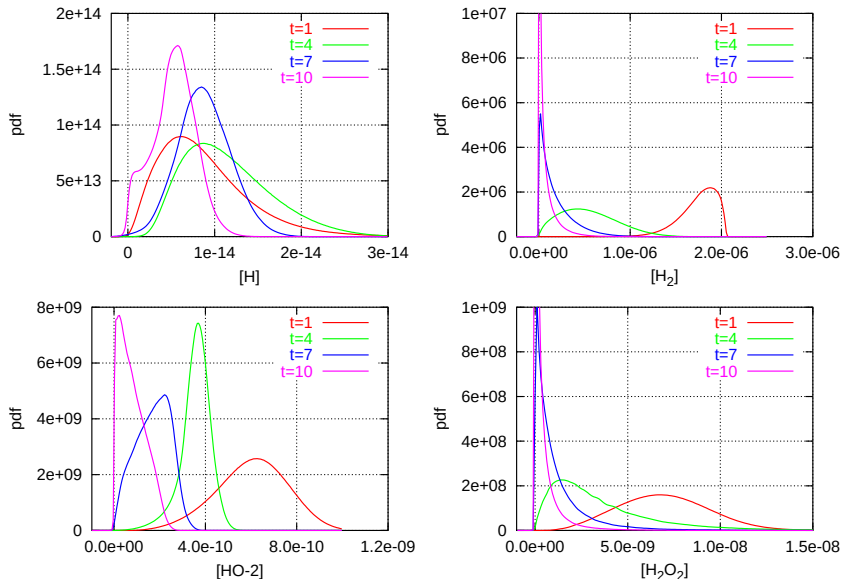

Figure 21: Pdfs of [H], [H_2], [HO_2] and [H_2O_2] at different times, computed with $N_o = 1$ and $\epsilon_r = 0.005$.

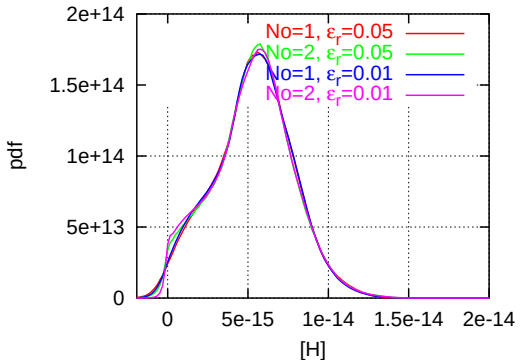

Figure 22: Pdfs of [H] for $N_o = 1$, 2 and $\epsilon_r = 0.05$ and 0.01.

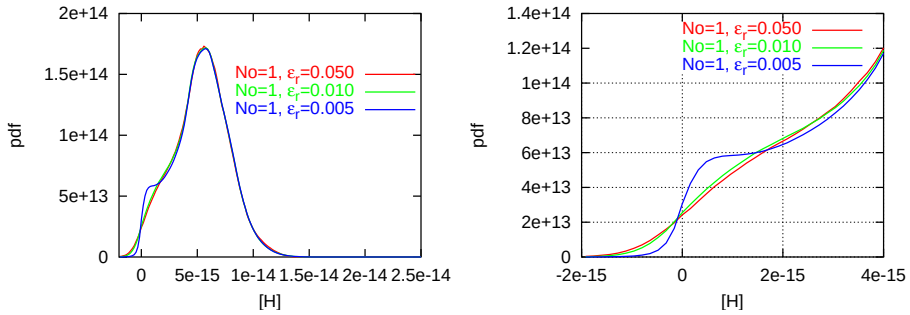

Figure 23: Left: comparison of the computed pdfs of [H] at $t = 10$, for $N_o = 1$ and decreasing refinement threshold as indicated. Right: details of the previous pdfs in the neighborhood of [H] $= 0$.